Monthly Notices of the ROYAL ASTRONOMICAL SOCIETY

MNRAS **513,** 2019–2038 (2022) https://doi.org/10.1093/mnras/stac936
Advance Access publication 2022 April 7

The extended H I halo of NGC 4945 as seen by MeerKAT

Roger Ianjamasimanana [1,2,3★] B. S. Koribalski [4,5] Gyula I. G. Józsa,[2,3,6] Peter Kamphuis,[7] W. J. G. de Blok,[8,9,10] Dane Kleiner [11] Brenda Namumba,[2] Claude Carignan,[12,13,14] Ralf-Jürgen Dettmar,[7] Paolo Serra,[11] Oleg M. Smirnov,[2,3] Kshitij Thorat [15,16] Benjamin V. Hugo,[2,3] Athanaseus J. T. Ramaila,[3] Eric Maina,[2] Filippo M. Maccagni [11] Sphesihle Makhathini,[17] Lexy A. L. Andati,[2] Dániel Cs. Molnár,[11] Simon Perkins,[3] Francesca Loi [11] Mpati Ramatsoku[2,11] and Marcellin Atemkeng [2]

[1] *Instituto de Astrofísica de Andalucía (CSIC), Glorieta de la Astronomía, E-18008 Granada, Spain*
[2] *Department of Physics and Electronics, Rhodes University, PO Box 94, Makhanda 6140, South Africa*
[3] *South African Radio Astronomy Observatory, 2 Fir Street, Black River Park, Observatory, Cape Town 7925, South Africa*
[4] *Australia Telescope National Facility, CSIRO Astronomy and Space Science, PO Box 76, NSW 1710, Epping, Australia*
[5] *Western Sydney University, Locked Bag 1797, Penrith, NSW 2751, Australia*
[6] *Max-Planck-Institut für Radioastronomie, Radioobservatorium Effelsberg, Max-Planck-Straße 28, D-53902 Bad Münstereifel, Germany*
[7] *Ruhr University Bochum, Faculty of Physics and Astronomy, Astronomical Institute, D-44780 Bochum, Germany*
[8] *Netherlands Institute for Radio Astronomy (ASTRON), Postbus 2, NL-7990 AA Dwingeloo, the Netherlands*
[9] *Department of Astronomy, University of Cape Town, Private Bag X3, Rondebosch 7701, South Africa*
[10] *Kapteyn Astronomical Institute, University of Groningen, Postbus 800, NL-9700 AV Groningen, the Netherlands*
[11] *INAF - Osservatorio Astronomico di Cagliari, Via della Scienza 5, I-09047 Selargius (CA), Italy*
[12] *Department of Astronomy, University of Cape Town, Private Bag X3, Rondebosch 7701, South Africa*
[13] *Département de physique, Université de Montréal, Complexe des sciences MIL, 1375 Avenue Thérèse-Lavoie-Roux Montréal, Qc, H2V 0B3, Canada*
[14] *Laboratoire de Physique et de Chimie de l'Environnement, Observatoire d'Astrophysique de l'Université Ouaga I Pr Joseph Ki-Zerbo (ODAUO), BP 7021, Ouaga 03, Burkina Faso*
[15] *Department of Physics, University of Pretoria, Hatfield, Pretoria 0028, South Africa*
[16] *The Inter-University Institute for Data Intensive Astronomy (IDIA), Department of Astronomy, University of Cape Town, Private Bag X3, Rondebosch 7701, South Africa*
[17] *University of the Witswatersrand, 1 Jan Smuts Avenue, Braamfontein 2000, Johannesburg, South Africa*

Accepted 2022 March 31. Received 2022 March 10; in original form 2021 March 18

ABSTRACT

Observations of the neutral atomic hydrogen (H I) in the nuclear starburst galaxy NGC 4945 with MeerKAT are presented. We find a large amount of halo gas, previously missed by H I observations, accounting for 6.8 per cent of the total H I mass. This is most likely gas blown into the halo by star formation. Our maps go down to a 3σ column density level of 5×10^{18} cm^{-2}. We model the H I distribution using tilted-ring fitting techniques and find a warp on the galaxy's approaching and receding sides. The H I in the northern side of the galaxy appears to be suppressed. This may be the result of ionization by the starburst activity in the galaxy, as suggested by a previous study. The origin of the warp is unclear but could be due to past interactions or ram pressure stripping. Broad, asymmetric H I absorption lines extending throughout the H I emission velocity channels are present towards the nuclear region of NGC 4945. Such broad lines suggest the existence of a nuclear ring moving at a high circular velocity. This is supported by the clear rotation patterns in the H I absorption velocity field. The asymmetry of the absorption spectra can be caused by outflows or inflows of gas in the nuclear region of NGC 4945. The continuum map shows small extensions on both sides of the galaxy's major axis that might be signs of outflows resulting from the starburst activity.

Key words: instrumentation: interferometers – methods: data analysis – galaxies: spiral.

1 INTRODUCTION

Starburst galaxies are characterized by their intense burst of star formation over a short period (Coziol 1996). Their star formation rates (SFRs) range from ∼10 to ∼1000 M$_\odot$ yr^{-1}. There are subclasses of starburst galaxies; those with a vigorous nuclear star formation, e.g. NGC 4945, NGC 253, NGC 660, NGC 1068, NGC 1365, NGC 1808, NGC 3079 (Koribalski 1996; Emig et al. 2020), and those that have a more distributed star formation mode, e.g. NGC 4631 (Irwin et al. 2011, 2012). This paper focuses on the study of the edge-on nuclear starburst galaxy NGC 4945. For simplicity,

★ E-mail: ianjamasimanana26@gmail.com, ianja@iaa.csic.es

we will refer to it simply as a starburst galaxy throughout the paper. The high levels of star formation in the nuclear region of starburst galaxies are thought to be due to gas accretion on to the centre, induced by bars, galaxy interactions or past merging events (Ishizuki et al. 1990; Ott et al. 2001; Lucero et al. 2015). Starburst galaxies have stellar populations dominated by massive stars, which transfer a significant amount of energy into the interstellar medium and, as a result, shape the gas distribution and kinematics of the galaxies (Freyer, Hensler & Yorke 2003; Zhang et al. 2018). Simulations show that star formation can drive the gas out of the disc plane, mostly as ionized gas. The gas eventually cools and rains back to the disc, fuelling future episodes of star formation. This so-called *galactic fountain model* (Shapiro & Field 1976) is consistent with observations of starburst galaxies. For example, extra-planar gas has been observed in the starburst galaxy NGC 4945 (Venturi et al. 2018) and its twin NGC 253 (Boomsma et al. 2005; Lucero et al. 2015), as well as the dwarf starburst galaxy M 82 (Martini et al. 2018). Edge-on galaxies offer a better way to study the vertical distribution of the gas compared to galaxies seen more face-on. For example, deep Westerbork Radio Telescope (WSRT) H I observations of the edge-on galaxy NGC 891 by Oosterloo, Fraternali & Sancisi (2007), labelled as a quiescent starburst galaxy by Temple, Raychaudhury & Stevens (2005), show large quantities of extra-planar gas, extending up to a vertical distance of 22 kpc. Thus, observations of the gas content of starburst galaxies are important in the studies of the mechanisms that initiate and regulate starburst activity.

The neutral atomic hydrogen gas (H I) remains the best tracer of the overall gas distribution and kinematics in galaxies. This is because H I can be traced out to a considerable distance from the galactic centre. Previous H I observations of nearby starburst galaxies have allowed the investigations of the possible triggering mechanisms of starburst. For example, the early H I observations of M 82 revealed that its velocity field showed strong deviations from circular motions, suggesting possible interactions with M81. Subsequent H I observations show filamentary structures connecting M 81, M 82, and NGC 3077, forming what is called the M 81-triplet (Yun, Ho & Lo 1994; de Blok et al. 2018; Sorgho et al. 2019). The interaction of M 82 with its neighbour is thought to have triggered its starburst activity (Mayya et al. 2006). H I observations of NGC 253 by Lucero et al. (2015) unveiled extra-planar gas emission out to a projected distance of ∼9 to ∼10 kpc from the nucleus and up to 14 kpc at the edge of the disc. Extra-planar gas has also been found for other starburst galaxies such as NGC 3079, NGC 4945, NGC 891 (Swaters, Sancisi & van der Hulst 1997; Ott et al. 2001; Fraternali et al. 2001; Boomsma et al. 2005; Oosterloo et al. 2007; Gentile et al. 2013; Marasco et al. 2019). Extra-planar gas is also common in normal star-forming spiral galaxies. For example, The Hydrogen Accretion in LOcal GAlaxieS survey (HALOGAS; Heald et al. 2011) found halo gas enclosing about 5–25 per cent of the total H I mass (Marasco et al. 2019), and moving slower than the gas in the disc of normal galaxies.

The amount of extra-planar H I found in starburst galaxies by previous observations is within the range found for normal galaxies (Boomsma et al. 2005; Lucero et al. 2015). With the improved sensitivity of MeerKAT, we aim to get high-quality H I imaging to trace possible halo gas that might have been missed by previous H I observations. In addition, we would like to compare the amount and distribution of the extra-planar H I we found for our starburst galaxy with those for normal galaxies. In this paper, we report high sensitivity H I observations of the nuclear starburst galaxy NGC 4945 with MeerKAT. Our H I map is about 2.5 times deeper in column density than previous ATCA mosaic imaging by LVHIS (Koribalski et al. 2018). NGC 4945 is a nearby edge-on starburst galaxy belonging to the Centaurus A group. The distance to NGC 4945 quoted in the literature varies between 3.8 and 8.1 Mpc (de Vaucouleurs 1964; Baan 1985; Bergman et al. 1992; Ott et al. 2001; Karachentsev et al. 2007; Mould & Sakai 2008). Here, we adopt a distance of 6.7 Mpc for easy comparison with the results of Ott et al. (2001) and other relevant studies. NGC 4945 is classified as a SB(s)cd galaxy (de Vaucouleurs et al. 1991). The central region of NGC 4945 harbours several physical processes. Apart from hosting a nuclear starburst, NGC 4945 is known to have a Seyfert 2 nuclei, which is thought to be responsible for some of its out-flowing gas (Done, Madejski & Smith 1996). Moreover, the nuclear region of NGC 4945 is among the richest sources of molecular lines, and therefore it has extensively been studied in the millimetre wavelengths (Dahlem et al. 1993; Henkel, Whiteoak & Mauersberger 1994; Curran et al. 2001; Ott et al. 2001; Hitschfeld et al. 2008; Hagiwara et al. 2016; Henkel et al. 2018). Measurements of different molecular abundance ratios in NGC 4945 suggest that its starburst activity is possibly reaching an advanced evolutionary stage (Curran et al. 2001; Cunningham & Whiteoak 2005). Some authors classified NGC 4945 as a post-starburst galaxy (Koornneef 1993). However, this was not confirmed by subsequent studies. The H I disc of NGC 4945 radially extends just a bit larger than the bright optical disc as shown by the ATCA map of Koribalski et al. (2018) and our MeerKAT data shown in this paper. This is peculiar for late-type spiral galaxies whose H I disc usually extends well beyond the optical disc (Ott et al. 2001; Koribalski et al. 2018). Other starburst galaxies that share this peculiarity include NGC 253 (Koribalski et al. 2018) and NGC 1433 (Ryder et al. 1996).

In this paper, we show high sensitivity maps of the radio continuum emission and the H I spectral line emission/absorption in NGC 4945 obtained with MeerKAT. Aided by the large field of view of MeerKAT, we obtained, for the first time, the most complete H I map of NGC 4945 with only a single pointing. This allows us to trace potential star formation outflows much more easily (Lucero et al. 2015; Ryder et al. 1996).

2 OBSERVATIONS AND DATA REDUCTION

NGC 4945 was observed with MeerKAT during 2019 May 24–26. The data was taken over two observing epochs using the *L*-band receiver, centred at 1284 MHz, with a bandwidth of 856 MHz divided into 4096 channels (44 km s^{-1} in velocity resolution). The compact radio sources PKS 1934–63, PKS 0408–65, and J1331+3030 were used as the bandpass calibrators, and J1318–4620 as the gain calibrator. Each observing run starts and ends with the bandpass calibrator, which was tracked every 2 h. The target and the gain calibrator were tracked one after the other. Thus, we spend 10 min on bandpass every 2 h, within which we cycle through 15-min target exposure and 2-min gain calibrator observation. This results in a total observing time of 15 h 50 min, during which 12 h 50 min were spent on the target.

The CARACal[1] (Józsa et al. 2020) data-reduction pipeline was used to produce a spectral-line data cube and a continuum image ready for scientific analysis. Based on PYTHON/STIMELA[2] scripts, CARACal incorporates many tasks from standard data-reduction software, e.g. CASA (McMullin et al. 2007), MEQTREES (Noordam J. E. & Smirnov O. M. 2010), CUBICAL (Kenyon et al. 2018), and

[1] https://github.com/caracal-pipeline/caracal
[2] https://github.com/ratt-ru/Stimela/wiki

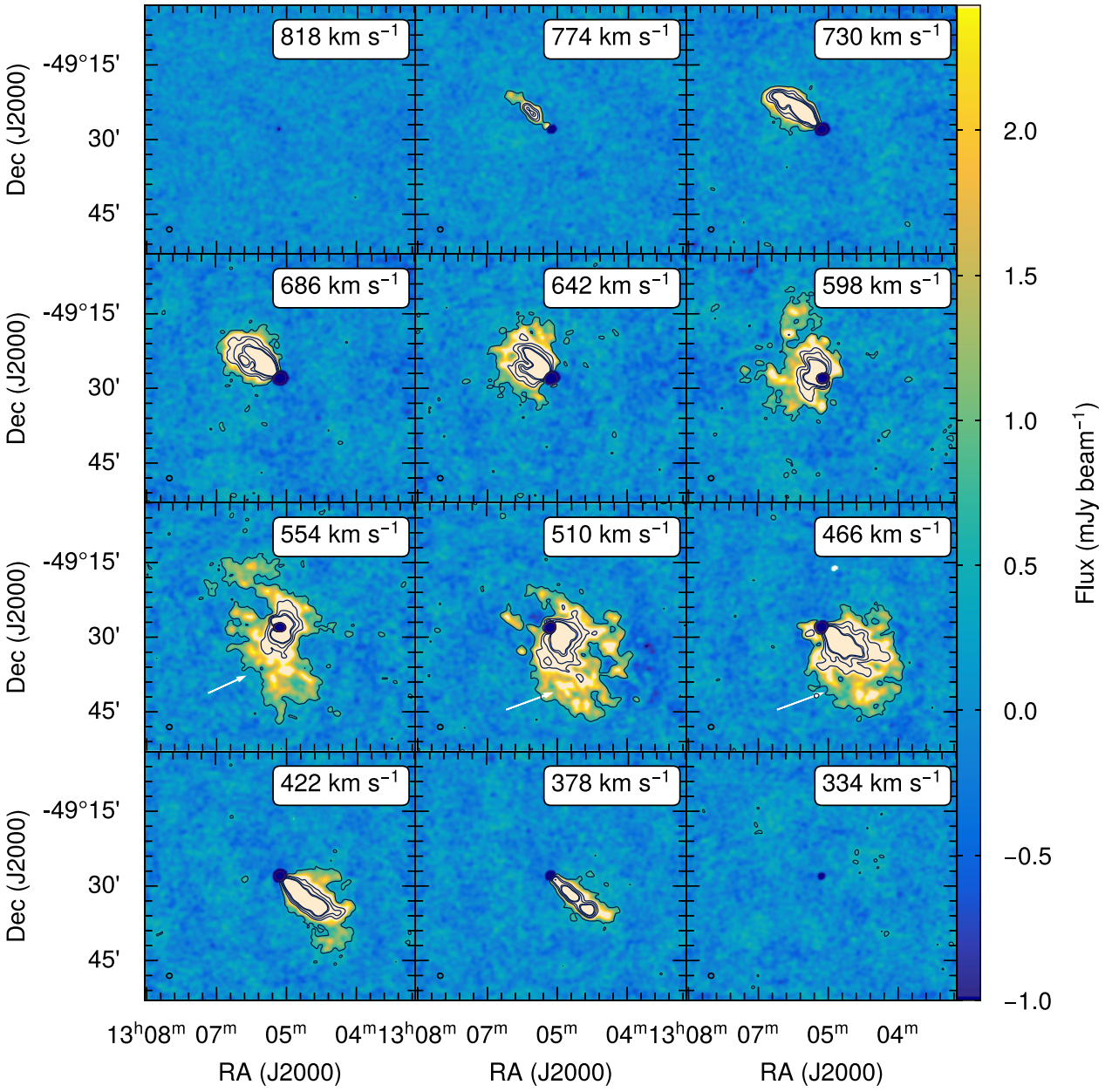

Figure 1. MeerKAT H I channel maps of the nearby starburst galaxy NGC 4945, smoothed to a resolution of 60 arcsec. The contour levels are (–10, –50, –90, –130, –170, –110, –150, 3, 20, 40, 80, 100) × rms where the rms is 0.2 mJy beam^{-1}. The red contours show the absorption in the centre of the galaxy. The white arrows indicate some of the previously unseen halo gas mentioned in the text. The black circles at the bottom left-hand corner of each panel show the size of the beam (FWHM = 60 arcsec).

SOFIA (Serra et al. 2015), which can be run sequentially using a YAML (a human-readable data-serialization language) configuration file through which the users can control which tasks need to be run/turned off and in which order. CARACal can perform all the standard data-reduction steps of radio astronomical data, from flagging, calibration to imaging. CARACal is written in PYTHON and uses container-based data processing technologies such as Singularity, Docker, uDocker, or Podman, allowing it to run across different platforms. Although CARACal was initially developed to reduce data from MeerKAT, its scope has been broadened to allow data processing from any other radio telescopes. Examples of peer-reviewed papers using CARACal include Ianjamasimanana et al. (2020), de Blok et al. (2020), and Józsa et al. (2021).

We use a bandwidth of 30 MHz, centred around the H I line of NGC 4945. To produce the final data used in this analysis, first, radio frequency interference (RFI) were flagged using the AOFlagger (Offringa 2012). Then, cross-calibration was performed using the CASA task *gaincal* to solve for the time-dependent delays (K) and complex gains (G) of each antenna, and the *bandpass* task to obtain the bandpass (B) solutions. After that, the data were passed through the CARACal selfcal worker to perform self-calibration. For that, five successive WSClean (Offringa et al. 2014) imaging loops and phase-only gain corrections with CubiCal (Kenyon et al. 2018) were used. The clean mask threshold was iteratively lowered in each step until the continuum residual was noise-like. Finally, to produce the spectral line data cube, first, the continuum clean model produced

in the self-calibration step was subtracted from the calibrated data. After that, the CASA task *mstransform* was used to fit the remaining continuum with a polynomial function of order one and subtract it from the data. The continuum subtracted data were then cleaned using WSClean in its multiscale mode. A robust parameter of 0 was used, which resulted in a synthesized beam size of 7.5×6.4 arcsec^2. The rms noise of the final data cube is 0.085 mJy beam^{-1}, which is close to the expected theoretical noise of 0.070 mJy beam^{-1}, calculated from the radiometer formula and using a penalty factor of 1.5 to account for robust weighting. We further smooth the data to a 60 arcsec circular beam with the MIRIAD (Sault, Teuben & Wright 1995) task CONVOL. The rms noise of the 60 arcsec cube is 0.20 mJy beam^{-1}. Note that the detected halo gas reported in this paper is already clearly visible even at the highest spatial resolution (i.e. 7.5×6.4 arcsec^2) as shown in the Appendix. One may think that smoothing the cube to a larger beam after cleaning could result in large-scale wings and ripples in the dirty psf mimicking halo gas. However, our use of a multiscale cleaning, which uses different size scales, already addresses these issues. In addition, we have also used a mask produced by SoFiA during an initial imaging step to produce our final image. We show the low-resolution version in this paper to emphasize the halo gas and speed up the processing time for the 3D kinematic modelling. Thus, the results presented in the main section of the paper are those using the smoothed data cube unless stated otherwise in the paper. In addition, we made two versions of the radio continuum map of NGC 4945, one at a resolution of 17.6 $\times$ 15.8 arcsec^2, and another one at a resolution of 7.3×6.2 arcsec^2. This paper presents the continuum map at 17.6×15.8 arcsec^2 unless otherwise stated.

3 RESULTS

3.1 H I channel maps and global profile

We present the MeerKAT H I channel maps of the starburst galaxy NGC 4945 in Fig. 1. They reveal previously unseen fluffy faint H I emission surrounding and/or connected to the main disc of the galaxy. They are most clearly visible at channels V = (466, 510, 554, 598)km s^{-1} as indicated by the white arrows in the figure. We are unsure about their exact origin due to the lack of velocity resolution. We could not model them properly and have excluded them in our modelling presented in Section 3.3. We will discuss its possible origin in Section 4. We present the global H I profile of NGC 4945 in Fig. 2. The global profile is double-horned, typical of spiral galaxies with a flat rotation curve. In addition, it is asymmetric, with the approaching side having higher peak flux-density than the receding side. By fitting the profile using the busy function (BusyFit; Westmeier et al. 2014), we find a W_{50} (full width at 50 per cent of the peak flux) of 359 km s^{-1}, a W_{20} (full width at 20 per cent of the peak flux) of 397 km s^{-1}, and a systemic velocity of $v_{\rm sys}$ = 530 km s^{-1}. Note that the $v_{\rm sys}$ we use throughout the rest of the paper is the one we estimated from the tilted-ring modelling described in Section 3.3. From the H I intensity map, we measure a total H I flux of 509 Jy km s^{-1}. Single dish observations using the Parkes radio telescope resulted in a measured flux of 319 Jy km s^{-1}, $v_{\rm sys}$ = 563 km s^{-1}, and $W_{50} = 361$ km s^{-1} (HIPASS; Koribalski et al. 2004). The ATCA mosaic imaging by Koribalski et al. (2018) yielded a total flux of 405.3 Jy km s^{-1}. Thus, we detect 37 and 20 per cent more flux than the HIPASS and the LVHIS surveys, respectively. Using our adopted distance of 6.7 Mpc, we measured a total H I mass of 5.4×10^9 M$_\odot$. Recall that here only a single pointing was required to map the extended H I disc of NGC 4945, which is thanks to the large primary beam of MeerKAT. Due to the strong H I absorption present towards the nuclear region of the galaxy, the estimated total mass represents the H I mass seen in emission but not the total H I mass.

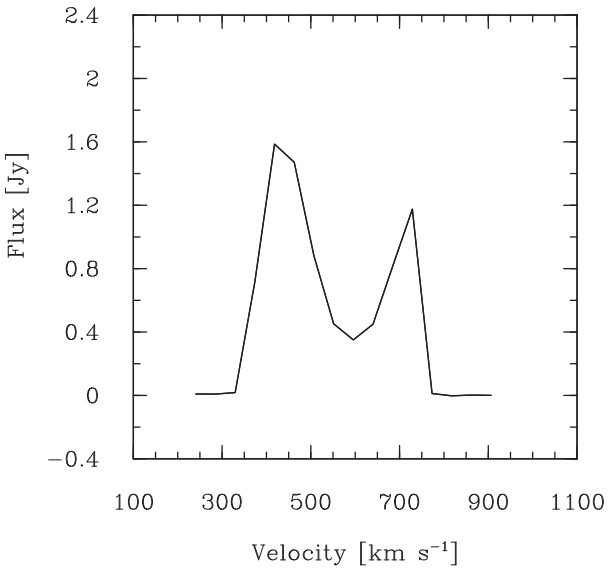

Figure 2. MeerKAT Global H I profile of NGC 4945.

3.2 H I moment maps

To get a map of the integrated H I intensity and velocity field of NGC 4945, we calculate the zeroth- and the first-moment of its spectrum. To locate an area containing only genuine emission, we create a mask by smoothing the data cube to a resolution of 75 arcsec. This cube is then used as a mask for the 60 arcsec cube to select pixels above a set level of three times the rms noise of the lower resolution cube. The moment calculations are done with the masked data cube. We show the integrated intensity map (moment zero) and velocity field (moment one) of the H I emission in Fig. 3. The moment zero map reveals previously undetected faint H I emission, extending out to a major axis diameter of 32 arcmin and a minor axis diameter of 18 arcmin (62×35 kpc), measured at a position angle of 45°, and at a mass surface density level of 0.02 M$_\odot$ pc^{-2}. An illustration of how these numbers are derived is shown in the Appendix. The distribution is clearly asymmetric, with the south-eastern side having much more faint extended emission than the rest of the galaxy.

The observations by the LVHIS survey (Koribalski et al. 2018) provide the most sensitive H I maps of NGC 4945 in the literature. On the receding side, the radial extent of the moment zero map of our MeerKAT H I observation is similar to the extent found by LVHIS as it also ends at the edge of the optical disc as shown in Fig. 3. However, on the approaching side, our map radially extends slightly further than that of LVHIS. In addition, we find significantly more gas in the lower left quadrant of the galaxy than what was detected by the LVHIS. This is due to our improved sensitivity, going down to a 3σ column density level of 5×10^{18} cm^{-2} at a 44 km s^{-1} velocity resolution and a 60 arcsec beam, compared to 1.2×10^{19} cm^{-2} for LVHIS. The finger-like structures seen on both sides of the major axis of NGC 4945 were already apparent on the LVHIS map, though they are more clearly visible here. The area where H I absorption occurs appears as blanked pixels in Fig. 3. There is a central concentration of high-density gas extending symmetrically with respect to the minor axis towards each side of the galaxy. The disc velocity field shows the

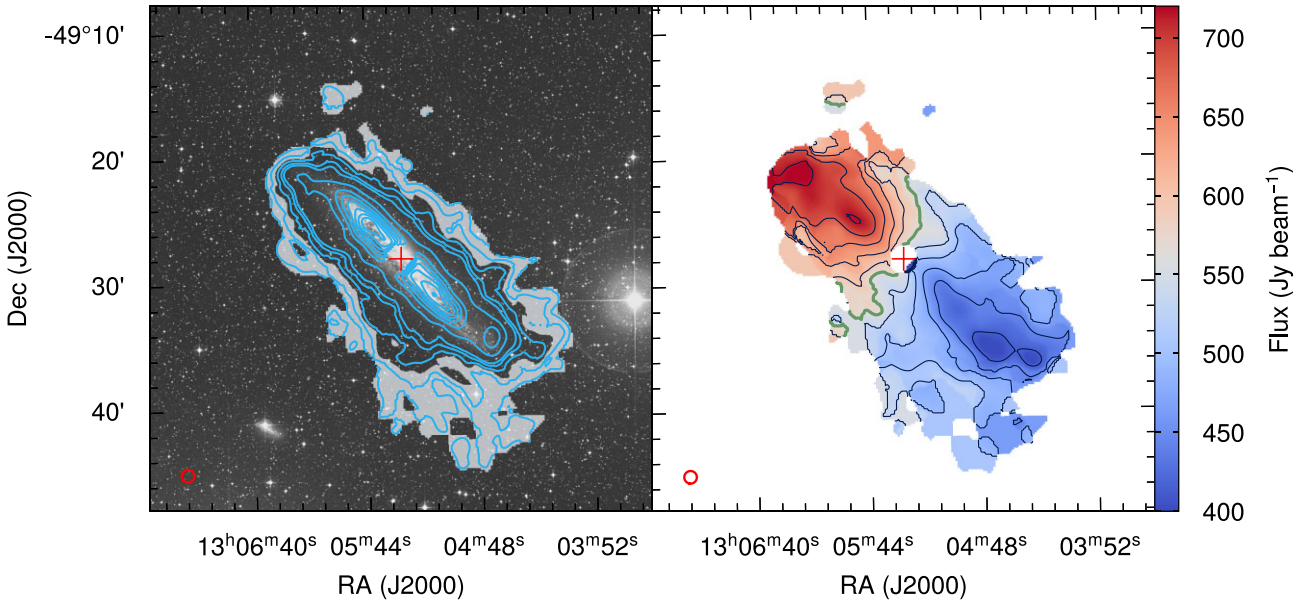

Figure 3. Left-hand panel: MeerKAT H I column density map of the starburst galaxy NGC 4945 overlaid on to a DSS2 *B*-band optical image shown in grayscale. The contour levels are (4.1×10^{19}, 1.0×10^{20}, 2.0×10^{20}, 3.1×10^{20}, 4.1×10^{20}, 1.0×10^{21}, 2.0×10^{21}, 3.1×10^{21}, 4.1×10^{21}, 5.1×10^{21}, 6.1×10^{21}, 7.2×10^{21}) cm^{-2}. We show in grayscale the column density values below 1.5×10^{20} cm^{-2} to highlight the halo gas. Right-hand panel: MeerKAT H I velocity field of NGC 4945. The contour levels are $V_{\rm sys} \pm 180\,\mathrm{km\,s^{-1}}$ in step of $30\,\mathrm{km\,s^{-1}}$, where $V_{\rm sys} = 565\,\mathrm{km\,s^{-1}}$ and is indicated by the green contour. The red crosses indicate the kinematic center derived by TIRIFIC. The red circles at the bottom left-hand corner of each panel show the size of the beam (FWHM = 60 arcsec).

regular spider pattern, which indicates a rotationally supported system. There are kinks in the iso-velocity contours, which have usually been attributed to non-circular motions caused by bars, spiral arms, or star formation. In addition, irregular patterns are seen in the South-Eastern side where the faint extended emission is detected. Finally, the iso-velocity contours appear to be twisted on the approaching and the receding sides, indicating a warp-like morphology.

H I absorption

H I absorption is seen against the bright radio continuum emission in the nuclear region of NGC 4945. Most notably, the H I absorption is seen throughout the entire velocity range of the H I emission of the galaxy. As shown in Fig. 1, H I absorption is present even in channels without H I emission. We show the H I absorption line at the peak of the nuclear continuum emission in Fig. 4. It has a peak velocity of 640 $\mathrm{km\,s^{-1}}$, a peak flux-density of –1 $\mathrm{Jy\,beam^{-1}}$, and a wide velocity extent ranging from 375–777 $\mathrm{km\,s^{-1}}$. The profile has a W_{50} of 226 $\mathrm{km\,s^{-1}}$ and W_{20} of 315 $\mathrm{km\,s^{-1}}$. This is within the range of broad H I absorption profiles as categorized by Geréb et al. (2015). They found that broad H I absorption profiles tend to be asymmetric and most likely arise from either a highly turbulent H I gas or a fast rotating ring. Here, also we find the H I absorption profile of NGC 4945 to be broad and asymmetric. To quantify the asymmetry of the profile, we use the following relation by Geréb et al. (2015)

$$a_v = max\left(\frac{v_{\rm FW20R} - v_{\rm HIpeak}}{v_{\rm HIpeak} - v_{\rm FW20B}}, \left(\frac{v_{\rm FW20R} - v_{\rm HIpeak}}{v_{\rm HIpeak} - v_{\rm FW20B}}\right)^{-1}\right), \quad (1)$$

where $v_{\rm H\,I\,peak}$ is the velocity at the position of the peak, and $v_{\rm FW20R}$ $v_{\rm FW20B}$ are the velocities at 20 per cent of the peak flux on the receding and the approaching side of the profile with respect to its peak position, respectively. As explained by Geréb et al. (2015), the maximum value between the velocity ratio and its reciprocal ensures

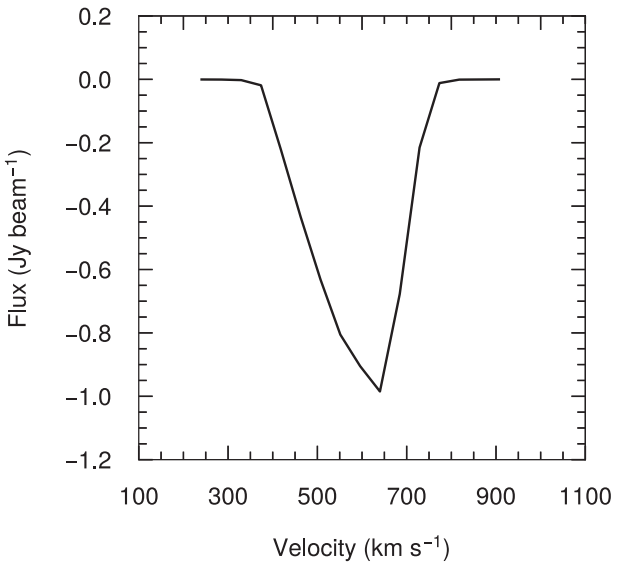

Figure 4. H I absorption profile at the central peak of the nuclear continuum in NGC 4945.

that the asymmetry value is always greater than 1, independent of whether the line is skewed to the left or to the right. We find a_v= 2.37. This value is consistent with the asymmetric parameter values found by Geréb et al. (2015) for galaxies with FW20 $\geq$ 300 $\mathrm{km\,s^{-1}}$. In Fig. 5, we show the velocity field of the H I absorption in the central region of NGC 4945 using the high resolution data cube at 7.5 × 6.4 arcsec^2. The velocity field indicates a clear solid-body rotation pattern, very similar to the radio recombination lines (RRL) velocity field derived by Roy et al. (2010) and the H I absorption velocity field by Ott et al. (2001). Thus, the broad H I absorption

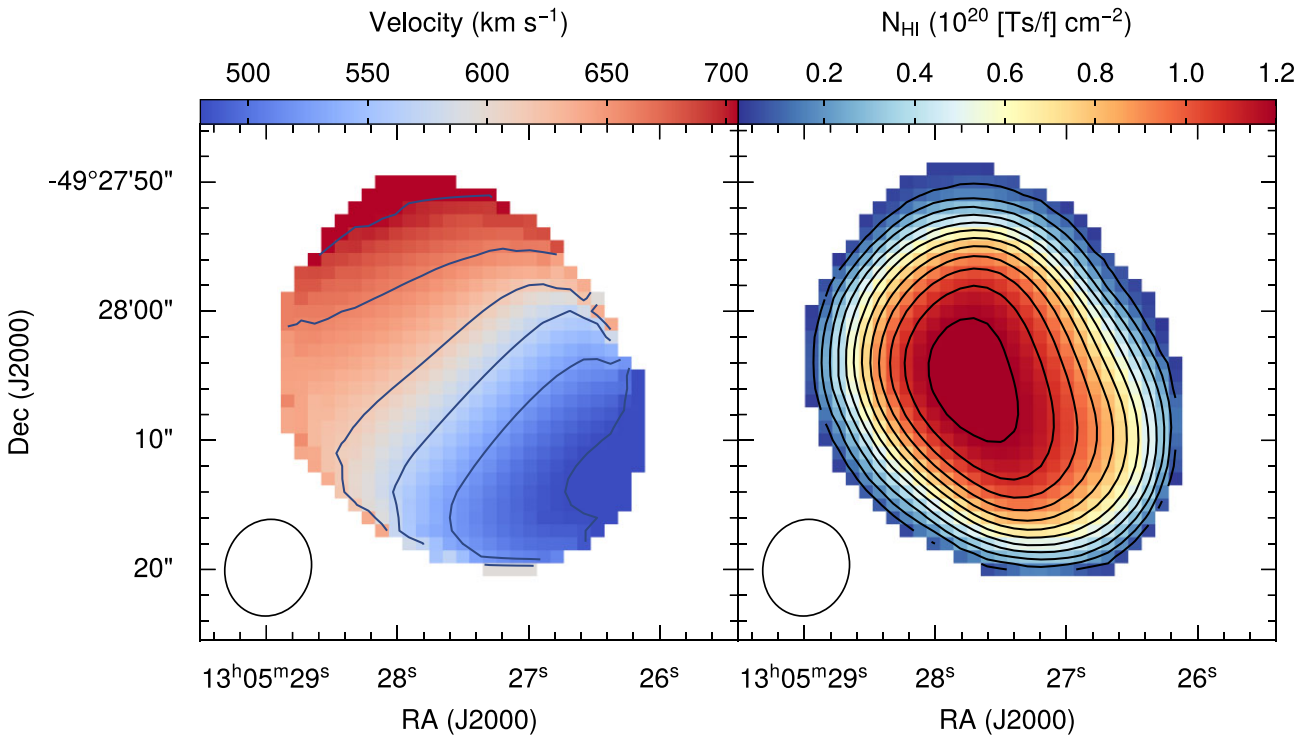

Figure 5. Left-hand panel: Velocity field of the H I absorption in the central region of NGC 4945, using the data cube at 7.5 × 6.4 arcsec^2 resolution. The contour levels are (480, 525, 570, 615, 660, 705) km s^{-1}. Right-hand panel: column density map of the H I absorption in the central region of NGC 4945, using the data cube at 7.5 × 6.4arcsec^2 resolution. The contour levels are 0.1–1.2 in step of 0.1 in units of 10^{20} [Ts/f] cm^{-2}. The black ellipses in each panel show the beam.

lines in NGC 4945 cannot be caused by a highly turbulent gas but rather by a fast rotating ring of neutral gas around a central AGN. As explained by Koribalski, Dickey & Mebold (1993), there would be no systematic shift in velocity with position if the broad lines were caused by gas moving at random velocity. However, outflows or inflows may be responsible for the asymmetry in the absorption lines of the galaxy. See also similar cases in NGC 1808 (Koribalski et al. 1993) and other nearby spiral galaxies (Koribalski 1996). Another evidence for the existence of a fast rotating ring around the central AGN of NGC 4945 includes the detection of a megamaser with a broad velocity range (400–1100 km s^{-1}) by Humphreys et al. (2016).

We show the column density map of the H I absorption, $N_{\rm HI}$, in the central region of NGC 4945 in Fig. 5. The column density was derived using the following equation

$$N_{\rm H\,I} = 1.822\,43 \times 10^{18}\, Ts\, \frac{F_{\rm H\,I,\ abs}}{f\, F_{\rm H\,I,\ cont}}\, \Delta v, \qquad (2)$$

where Ts is the spin temperature of hydrogen atoms in K, $F_{\rm H\,I,\ abs}$ is the flux from the H I absorption lines in Jy beam^{-1}, $F_{\rm H\,I,\ cont}$ is the flux from the 21-cm radio continuum in Jy beam^{-1}, f is the covering factor, and Δv is the channel width in km s^{-1}. We find $N_{\rm H\,I} = 1.7 \times 10^{18} - 1.3 \times 10^{20}$ [Ts/f cm^{-2}]. The spin temperature is a poorly constrained parameter and depends on a lot of excitation mechanisms such as the cosmic microwave background (CMB) radiation, collisional excitation, and Lyα radiation (Field 1959). The column density of the H I emission in the central region of NGC 4945 is well above the threshold value for cold neutral medium formation (CNM), $N_{\rm H\,I} \gtrsim 2 \times 10^{20}$ cm^{-2} (Kanekar, Braun & Roy 2011). Thus, we expect the H I in the central region of NGC 4945 to be predominantly in the cold phase with Ts $\lesssim$ 500 K (Kanekar et al. 2011). This is supported by the presence of molecular gas in NGC 4945 as reported by Ott et al. (2001) and the high rate of nuclear star formation, indicating an enhanced atomic-to-molecular conversion process.

3.3 Kinematic modelling

To model the H I gas distribution and kinematics in NGC 4945, we use the 3D tilted ring fitting software FAT (Kamphuis et al. 2015) and TIRIFIC (Józsa 2007). FAT is built upon TIRIFIC but was designed to be run in a fully automated manner. FAT and TIRIFIC model a galaxy as a set of concentric rings with kinematic and orientation parameters that can either be varied or held fixed with radius. Each ring is characterized by its centre position, inclination angle with respect to the line of sight, position angle of the receding major axis, systemic velocity, rotation velocity, velocity dispersion, vertical thickness, and surface brightness distribution. The disc can be segmented and fitted independently, allowing the user to e.g. fit the approaching and the receding halves independently. TIRIFIC can be used to model non-axisymmetric features and large-scale motions such as those induced by the presence of bars. This can be achieved by including harmonic distortions in velocity and/or surface brightness distribution while modelling.

3.3.1 Modelling strategy

To model NGC 4945, first, we make a base model with FAT. Then, we use the output model of FAT as input for TIRIFIC to refine the model and identify features not captured by FAT. We start with the simplest possible model, i.e. a model with the geometric parameters, systemic velocity, and velocity dispersion held fixed with radius, but allowing for the surface brightness and the rotation velocity to vary as a function of radius. We visually compare the resulting model with

Table 1. Tilted-ring parameters not varying with radius.

NGC 4945 TIRIFIC model parameters that are constant with radius			
Parameter	Symbol	Value	Unit
Model centre	XPOS	$13.0^{h}\,05.0^{m}\,28\overset{s}{.}0 \pm 00\overset{s}{.}0$	
(J2000)	YPOS	$-49.0^{d}\,28.0^{m}\,05\overset{s}{.}8 \pm 00\overset{s}{.}4$	
Systemic velocity	VSYS	565 ± 6	km s^{-1}
Thickness	Z0	42.6 ± 3.0 arcsec	
Dispersion	CONDISP	23.0 ± 1.5	km s^{-1}

the data and add/vary one or more parameters if the simpler model does not adequately describe the data. As briefly mentioned before, we excluded the faint emission in the fitting as we failed to properly model it due to our coarse velocity resolution of 44 km s^{-1}. We will discuss more the properties of the anomalous gas in Section 3.4. Thus, in addition to applying a mask based on the 75 arcsec data as described in the previous section, we create an elliptical region surrounding the main disc of the galaxy and use the MIRIAD task IMMMASK to mask out areas outside the ellipse. We put zeros in the areas that have been masked out. The masked data cube is then fed into TIRIFIC for the modelling. Note that due to the presence of the central absorption, which has been masked out, the fitting in the central part (about an arcminute in radius) is uncertain. Thus, we refrain from doing mass modelling.

3.3.2 Model parameters

Our final best-fitting model is a model where we fit the approaching and receding sides separately as described below.

(i) The following parameters have been kept constant with radius:

(a) Centre position: XPOS, YPOS, XPOS_2, YPOS_2
(b) Systemic velocity: VSYS, VSYS_2
(c) Global dispersion: CONDISP (this does not vary with radius by default, and should not be confused with the SDIS parameter which can be varied with radius)
(d) Disc thickness: Z0, Z0_2

(ii) The following parameters have been allowed to vary with radius:

(a) Rotation velocity: VROT, VROT_2
(b) Surface brightness: SBR, SBR_2
(c) Amplitude of harmonic distortions in surface brightness (first and second order): SM1A, SM1A_2; SM2A, SM2A_2
(d) Phase of harmonic distortions in surface brightness (first and second order): SM1P, SM1P_2; SM2P, SM2P_2
(e) Inclination: INCL, INCL_2
(f) Position angle: PA, PA_2

We show the parameters that are kept constant with radius in Table 1. The ones that vary with radius are shown in Fig. 6 and Table 2.

General properties

(i) We derive a flat rotation curve, typical of spiral galaxies. A fit to the following function (Boissier et al. 2003; Leroy et al. 2008)

$$v_{\rm rot}(r) = v_{\rm flat}\left[1 - \exp\left(1 - \frac{-r}{l_{\rm flat}}\right)\right], \quad (3)$$

gives the numbers quoted in Table 3, where $v_{\rm rot}(r)$ is the rotation curve, $v_{\rm flat}$ is the rotation velocity at the flat part of the rotation curve, $l_{\rm flat}$ is the length scale over which $v_{\rm rot}$ approaches $v_{\rm flat}$ (Leroy et al. 2008).

(ii) The position angle and inclination clearly indicate an outer warp in the approaching and the receding sides.

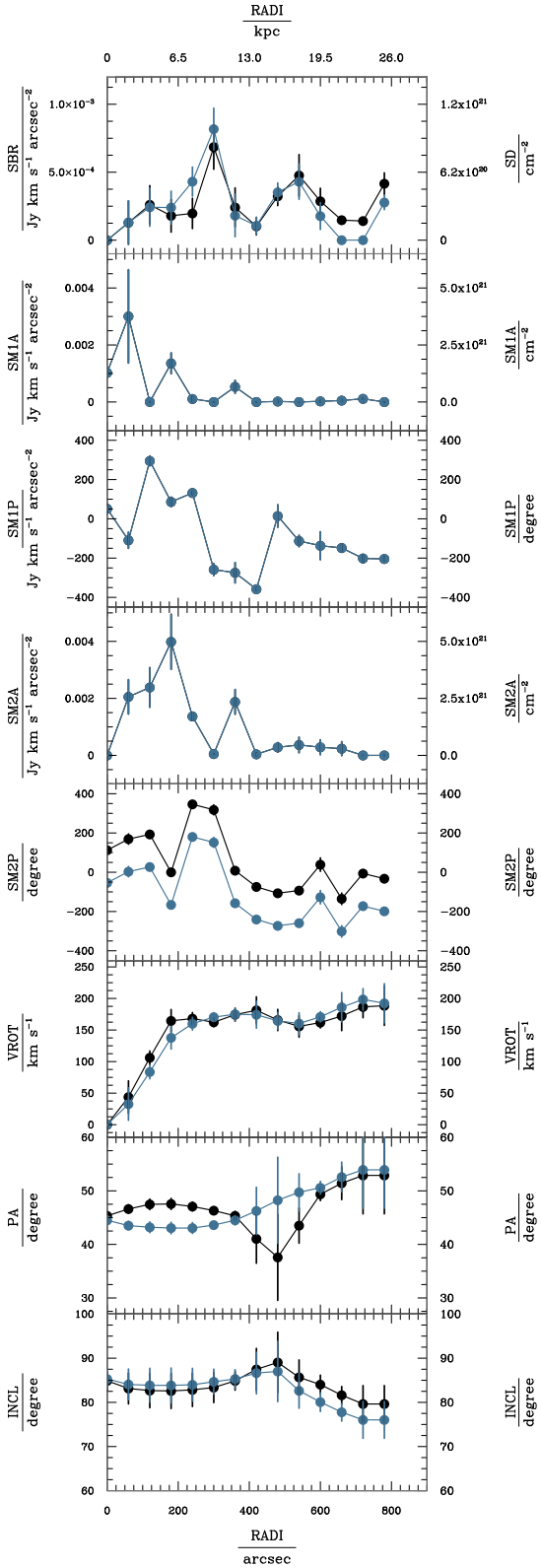

Figure 6. TIRIFIC model parameters of NGC 4945 that vary with radius, they are tabulated in Table 2. Black: approaching side, blue: receding side. For SM1A, SM1P, and SM2A, the black and the blue curves overlap.

Table 2. TIRIFIC model parameters of the NGC 4945 H I disc that vary with radius, also shown in Fig. 6.

RADI	SBR	ERR_SBR	SM1A	ERR_SM1A	SM1P	ERR_SM1P	SM2A	ERR_SM2A	SM2P	ERR_SM2P	VROT	ERR_VROT	PA	ERR_PA	INCL	ERR_INCL
0.	4.8e-08	4.9e-09	1.0e-03	1.8e-04	51.6	6.9	1.9e-07	3.5e-08	1.1e+02	8.5	0.	0.	45.3	0.8	84.9	2.1
60.	1.3e-04	1.6e-04	3.0e-03	1.6e-03	−109.	41.4	2.1e-03	6.0e-04	1.7e+02	26.2	43.8	25.7	46.6	0.8	83.1	3.5
120.	2.6e-04	1.4e-04	4.5e-06	5.1e-06	295.	25.2	2.4e-03	6.9e-04	1.9e+02	15.2	106.2	10.7	47.5	1.	82.7	3.9
180.	1.8e-04	1.2e-04	1.4e-03	3.7e-04	86.5	24.	4.0e-03	9.7e-04	7.9e-02	13.7	164.6	17.9	47.6	1.	82.6	4.
240.	2.0e-04	1.1e-04	1.1e-04	9.5e-05	132.	8.3	1.4e-03	1.5e-04	3.5e+02	13.2	168.1	9.7	47.1	0.8	82.8	3.8
300.	6.9e-04	1.6e-04	5.1e-07	4.8e-07	−258.5	30.2	5.0e-05	1.0e-05	3.2e+02	25.6	162.3	7.1	46.3	0.5	83.4	3.4
360.	2.4e-04	1.4e-04	5.3e-04	2.3e-04	−274.4	52.1	1.9e-03	4.3e-04	8.5e+00	5.4	174.3	10.3	45.3	0.8	84.9	2.1
420.	1.0e-04	6.4e-05	1.1e-06	1.5e-06	−358.2	7.	4.0e-05	4.7e-05	–7.4e+01	16.4	181.3	21.3	41.	4.6	87.5	4.7
480.	3.2e-04	6.9e-05	1.9e-05	3.5e-05	14.3	57.1	2.8e-04	1.6e-04	–1.1e+02	16.5	165.9	16.9	37.6	8.	89.	6.8
540.	4.8e-04	1.5e-04	1.0e-06	1.1e-06	−112.9	29.4	3.7e-04	2.7e-04	–9.3e+01	12.2	155.8	17.1	43.5	3.3	85.7	3.9
600.	2.9e-04	9.6e-05	2.4e-05	2.4e-05	−136.8	70.9	2.9e-04	2.6e-04	3.9e+01	34.4	161.8	8.6	49.4	1.2	84.	2.1
660.	1.5e-04	2.3e-05	5.1e-05	2.9e-05	−148.2	21.6	2.4e-04	2.4e-04	–1.4e+02	29.3	172.2	23.2	51.4	3.1	81.6	2.
720.	1.4e-04	1.8e-05	1.1e-04	2.1e-05	−201.6	17.1	6.0e-07	8.5e-08	–6.2e+00	11.7	186.7	17.2	52.9	7.2	79.6	4.2
780.	4.2e-04	8.0e-05	6.3e-07	1.1e-07	−204.	10.4	5.9e-07	9.6e-08	–3.3e+01	8.2	188.5	31.1	52.9	7.2	79.6	4.2
RADI	SBR_2	ERR_SBR_2	SM1A_2	ERR_SM1A_2	SM1P_2	ERR_SM1P_2	SM2A_2	ERR_SM2A_2	SM2P_2	ERR_SM2P_2	VROT_2	ERR_VROT_2	PA_2	ERR_PA_2	INCL_2	ERR_INCL_2
0.	4.9e-08	4.9e-09	1.0e-03	1.8e-04	51.6	6.9	1.9e-07	3.5e-08	−53.7	8.5	0.	0.	44.5	0.8	85.3	2.1
60.	1.3e-04	1.6e-04	3.0e-03	1.6e-03	−109.	41.4	2.1e-03	6.0e-04	3.1	26.2	32.7	25.7	43.5	0.8	84.1	3.5
120.	2.4e-04	1.4e-04	4.5e-06	5.1e-06	295.	25.2	2.4e-03	6.9e-04	26.9	15.2	83.5	10.9	43.2	1.	83.9	3.9
180.	2.4e-04	1.2e-04	1.4e-03	3.7e-04	86.5	24.	4.0e-03	9.7e-04	−165.9	13.7	137.7	17.9	43.1	1.1	83.9	3.9
240.	4.3e-04	1.1e-04	1.1e-04	9.5e-05	132.	8.3	1.4e-03	1.5e-04	180.3	13.2	160.	10.1	43.	1.	84.	3.7
300.	8.2e-04	1.5e-04	5.1e-07	4.8e-07	−258.5	30.2	5.0e-05	1.0e-05	151.9	25.6	170.4	7.1	43.6	0.5	84.7	2.9
360.	1.8e-04	1.6e-04	5.3e-04	2.3e-04	−274.4	52.1	1.9e-03	4.3e-04	−157.5	5.4	174.9	10.2	44.5	0.8	85.3	2.1
420.	1.1e-04	6.3e-05	1.1e-06	1.5e-06	−358.2	7.	4.0e-05	4.7e-05	−240.3	16.4	174.2	21.3	46.3	4.4	86.6	4.7
480.	3.5e-04	6.9e-05	1.9e-05	3.5e-05	14.3	57.1	2.8e-04	1.6e-04	−272.7	16.5	164.5	13.7	48.3	8.	87.	6.8
540.	4.3e-04	1.3e-04	1.0e-06	1.1e-06	−112.9	29.4	3.7e-04	2.7e-04	−259.1	12.2	160.3	17.1	49.7	3.5	82.6	4.
600.	1.8e-04	9.8e-05	2.4e-05	2.4e-05	−136.8	70.9	2.9e-04	2.6e-04	−127.2	34.4	170.9	8.3	50.6	1.2	80.1	2.1
660.	2.3e-07	1.4e-07	5.1e-05	2.9e-05	−148.2	21.6	2.4e-04	2.4e-04	−301.2	29.3	186.1	23.2	52.6	2.8	77.8	2.
720.	4.7e-07	5.6e-08	1.1e-04	2.1e-05	−201.6	17.1	6.0e-07	8.5e-08	−172.2	11.7	198.5	17.1	53.9	7.2	76.	4.2
780.	2.8e-04	5.3e-05	6.3e-07	1.1e-07	−204.	10.4	5.9e-07	9.6e-08	−198.6	8.2	192.4	31.1	53.9	7.2	76.	4.2

Table 3. Flat part of the TIRIFIC rotation curve.

	$v_{\rm flat}$ (km s^{-1})	$l_{\rm flat}$ (kpc)
Approaching side	177.5 ± 5.9	3.8 ± 0.6
Receding side	188.0 ± 7.1	5.3 ± 0.8

Note. $v_{\rm flat}$: the rotation velocity at the flat part of the rotation curve, $l_{\rm flat}$ is the length scale over which $v_{\rm rot}$ approaches $v_{\rm flat}$ (Leroy et al. 2008).

(iii) The surface brightness profile decreases towards the centre due to the presence of the absorption. It appears to be disturbed (irregular), most likely due to a bar.

Properties of the kinematic model

The approaching side shows a steeper velocity gradient than the receding side. This is already apparent in the velocity field. However, their maximum rotation velocities agree within the uncertainties. In addition, both sides have an outer warp. Moreover, there are differences in the radial variations of the surface brightness distribution. The receding side appears to be brighter in the inner discs and fainter in the outer discs compared to the approaching side. The amplitude and the phase of the first-order harmonic distortions in surface brightness for the two sides are similar, though.

3.3.3 TIRIFIC *model versus data*

We compare the H I channel maps from the TIRIFIC model data cube with the H I channel maps from the observed data cube in Fig. 7. Overall, the agreement is good, except close to the systemic velocity. This is expected due to the absorption in the centre and the effects of radial/streaming motions possibly related to a bar, which are not included in the modelling. We compare the H I moment maps from the TIRIFIC model with the H I moment maps from the observations in Fig. 8. The model recovers the overall gas distributions and kinematics. Local deviations exist, though. We also show the residual H I moment maps obtained by subtracting the model from the data in Fig. 8. The residual velocity field has a mean value of –1.4 km s^{-1}, an rms of 11.1 km s^{-1}, and a median absolute deviation of 9.5 km s^{-1}. The largest deviation is –92.1 km s^{-1}, however; there are only five pixels that have deviations above the channel spacing. We show the H I position–velocity diagrams from the TIRIFIC model and the observed data cubes in Fig. 9. Overall, they agree with each other. However, the position–velocity diagram from slice C shows the largest discrepancy between the model and the data. As mentioned before, this is mostly due to the central absorption that has been blanked and set to zero fluxes before performing the fit.

3.4 Halo gas in NGC 4945

3.4.1 *Properties of the halo gas*

As mentioned previously, our high-sensitivity observations have revealed the presence of previously unseen emission in the halo of NGC 4945. To highlight this, we show the position–velocity diagrams of NGC 4945 in Fig. 10. This clearly reveals the presence of two components: a bright H I disc with flat rotation curve, and a faint halo gas with velocities closer to systemic than the regularly rotating disc. As shown by all the position–velocity cuts, the halo gas has an asymmetric distribution. Halo gas with similar properties to the one we find for NGC 4945 has been reported in both normal and starburst galaxies (Fraternali et al. 2001; Lucero et al. 2015; Vargas et al. 2017). We will discuss the possible origin of the extra-planar gas in NGC 4945 in Section 4.

3.4.2 *Separating the halo gas from the disc*

Due to our limited velocity resolution, the individual H I profiles of NGC 4945 could not be decomposed into multiple Gaussian components as was done for NGC 253 by Lucero et al. (2015). To summarize, they visually inspected each PV slice aligned along the galaxy's major axis to spot any kinematically anomalous gas component. In addition, they interactively fitted three Gaussians to all the line profiles making each PV slice. In our case, even using two Gaussians to fit the profiles failed in most cases. Thus, to separate the anomalous H I from the galaxy's disc, we use the kinematic model data cube derived by TIRIFIC as outlined above to mask the main disc of the galaxy and isolate the kinematically anomalous gas. We show the location of the anomalous gas in Fig 11. We tried to derive the rotation curve of the anomalous gas separately but we failed to obtain reliable kinematics.

We found an H I mass of 3.7×10^8 M$_\odot$, which accounts for 6.8 per cent of the total H I mass of the galaxy. This is almost twice as large as the fraction of the anomalous gas found in NGC 253 (Lucero et al. 2015). However, despite being a starburst galaxy, the fraction of the anomalous component we find for NGC 4945 is still well within the range expected for normal disc galaxies. Marasco et al. (2019) performed a Bayesian Markov chain Monte Carlo (MCMC) kinematic fit to 11 normal disc galaxies from the HALOGAS survey and found that about 5 to 25 per cent of the H I gas in their sample reside in the halo of the galaxies. Here, we expected to see more extra-planar H I in NGC 4945 than in normal galaxies. This is because, as reported in the literature (e.g. Strickland & Stevens 2000; Heckman et al. 2000), the brief burst of intense star formation leads to the existence of superwind and multiple episodes of type II supernova explosions in starburst galaxies. The combined effects of these mechanisms are expected to drive more gas in the halo than seen in normal galaxies. However, as demonstrated by Heckman et al. (2000) and Heckman (2003), starburst-driven superwind could accelerate a cloud of gas to a velocity larger than the velocity needed to escape the gravitational potential of the host galaxy ($v_{\rm esc}$). This would *result* in a fraction of gas being driven to the surrounding intergalactic medium instead of ending up in the halo. Heckman et al. (2000) and Heckman (2003) demonstrated that the superwind's energy loss due to radiative cooling in starburst galaxies is not strong enough to halt this process. This may be why being a starburst galaxy does not simply translate to having more extra-planar H I than normal galaxies. The escaped gas could be in the ionized form or a tenuous gas, escaping the detection limit of the current emission line surveys.

It is not uncommon to find more halo gas on one side than on the other side of galaxies, and this is true for both normal and starburst galaxies. If we cut NGC 4945 into two halves, 20 per cent of the anomalous gas resides in the northern side of the minor axis, whereas 79 per cent of the halo gas resides in the southern side. Similarly, 42.4 per cent of the halo gas is located above the major axis and 57.6 per cent below the major axis of the galaxy. We have assumed a position angle of 45° for the calculation.

We highlight the velocity field of the anomalous component in Fig. 12. The iso-velocity contours of the halo gas are irregular, and in general, do not follow the overall rotation pattern of the main disc. If the gas is of a galactic fountain origin, which is plausible as NGC

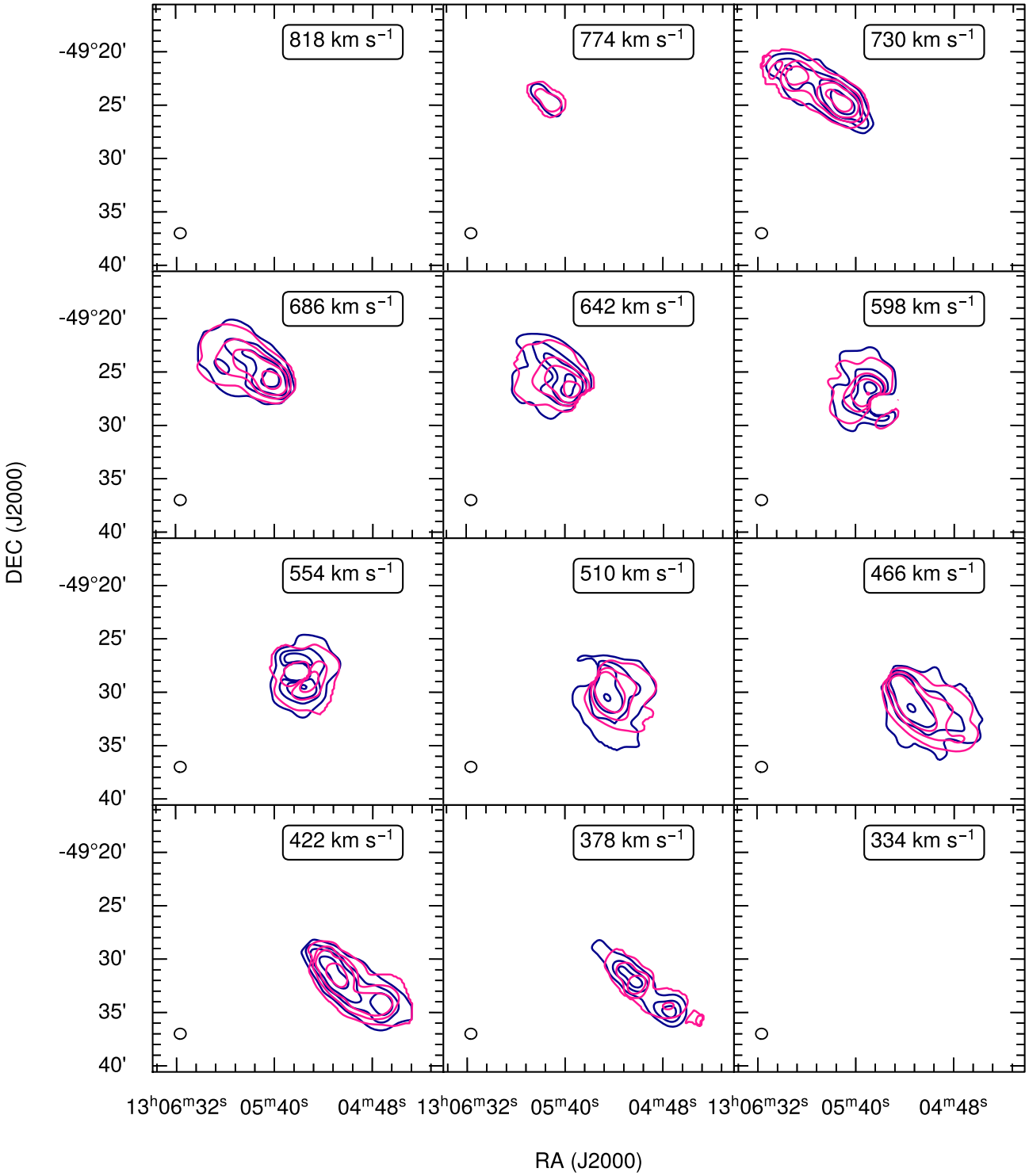

Figure 7. Comparison between the observed and the model H I data cubes of NGC 4945. Here, only the gas from the main disc of NGC 4945 is shown since we could not fit the gas in the halo as mentioned in the text. Blue: H I channel maps of observed data cube; deep pink: channel maps of TIRIFIC model data cubes. The contour levels are 0.0072, 0.0240, 0.0480, and 0.1200 Jy beam^{-1}. The black circles at the bottom left-hand corner of each panel show the size of the beam (FWHM = 60 arcsec).

4945 is a starburst galaxy, the irregularity of the velocity pattern of the halo gas indicates unsettled H I that will be accreted back on to the main disc of the galaxy at a later stage. An outer disc star formation could also cause such an irregularity. This can be investigated further using deeper H_α imaging. However, the star formation in NGC 4945 is so far known to be confined in its central part.

3.5 Radio continuum map

3.5.1 Distribution and total flux

To produce the 20-cm radio continuum map of NGC 4945, we selected a 100-MHz chunk of the raw data around the central

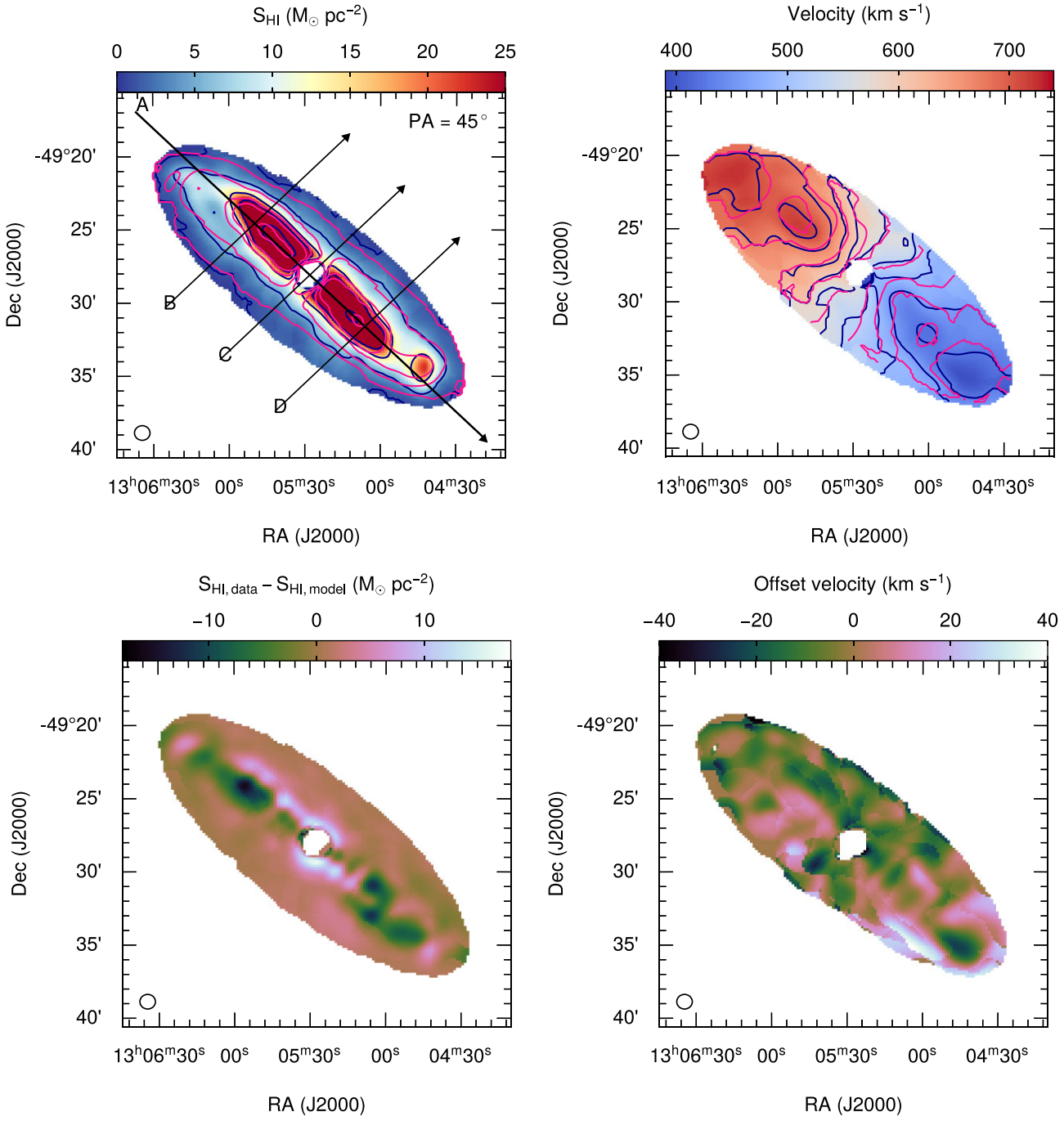

Figure 8. Comparison between the NGC 4945 H I moment maps from the observed and the model data cubes. Only the gas from the main disc of the galaxy is shown as we failed to model the gas in the halo of NGC 4945. Top left-hand panel: comparison between the observed H I surface density map and the TIRIFIC model surface density map. Arrows A, B, C, and D show slices from which the position–velocity diagrams shown in Figs 9 and 10 are taken. The intersection between arrows A and C represents the kinematic centre derived by TIRIFIC. The blue contours show the observed H I surface density. The deep pink contours represent the surface density map from the TIRIFIC model data cube. The contour levels are 1, 5, 15, 25, and 55 $M_\odot$ pc^{-1}. Top right-hand panel: first moment maps; the blue contours represent the observed velocity field, the deep pink contours show the model velocity field. The contour levels are $V_{sys} \pm 175$ km s^{-1} in steps of 35 km s^{-1}, where $V_{sys} = 565$ km s^{-1}. The residuals are shown in the bottom panels of the figure. Bottom left-hand panel: the difference between the observed H I surface density and the model H I surface density. Bottom right-hand panel: the difference between the observed velocity field and the model velocity field. The circles at the lower left-hand corners of each plot represent the size of the beam (FWHM = 60 arcsec).

emission of NGC 4945 to be reduced by CARACal. WSClean was used in its multiscale mode to account for the different size scales in the continuum map of NGC 4945. We let WSClean select the relevant scales automatically. Using a robust parameter of 0 and a Gaussian taper of FWHM = 15 arcsec, the final beam size is 17.6 × 15.8 arcsec^2. The rms of the final residual continuum image is 0.053 mJy beam^{-1}, whereas the rms of the continuum image is 0.06 mJy beam^{-1}. We show an overlay of the radio continuum map

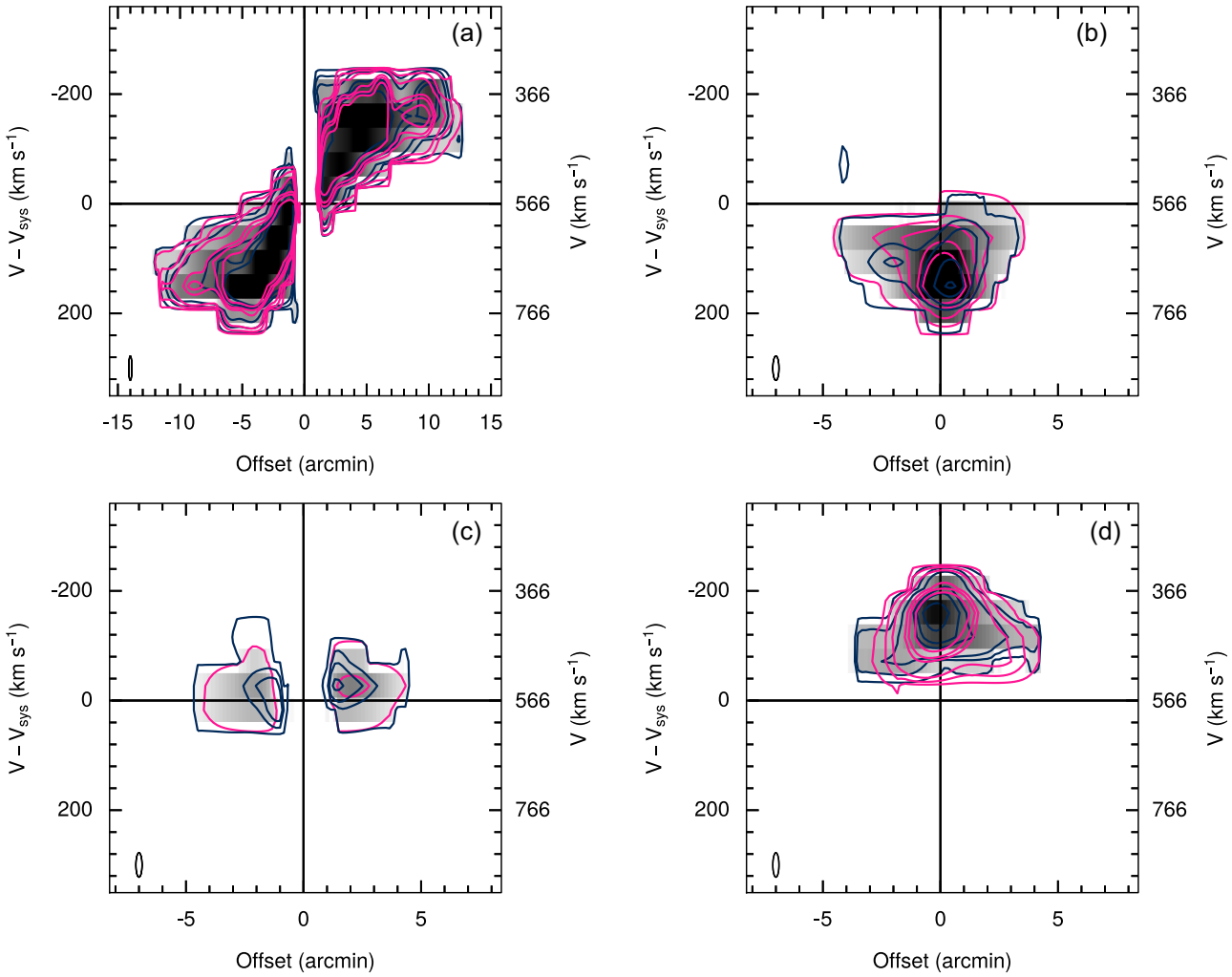

Figure 9. MeerKAT H I position–velocity diagrams from the model and the observed data cubes of NGC 4945 taken along slices A, B, C, and D as shown in Fig. 8. Here, also we only show the gas in the main disc of the galaxy since we could not model the gas in the halo as mentioned in the text. Blue contours: observed data. Pink contours: the TIRIFIC model. The contour levels are (0.00072, 0.01200, 0.02400, 0.04800, 0.07200) Jy beam^{-1}. The elongated ellipses at the lower left-hand corners of the plots show the size of the beam (FWHM = 60 arcsec, along the *x*-axis) and the channel spacing (along the *y*-axis).

of NGC 4945 on to a DSS *B*-band optical image in Fig. 13. The central continuum peaks at RA (J2000) = $13^{h}05^{m}27\overset{s}{.}4$ and Dec. (J2000) = $-49^{\circ}28'05''$, which agrees well with the centre position found by Whiteoak & Bunton (1985), Elmouttie et al. (1997), and Ott et al. (2001). The emission extends over 11.3 × 4.5 arcmin^2 at a position angle of 45° at a level of 1 mJy beam^{-1}. See the Appendix for an illustration on how these numbers were estimated. Using ATCA, Ott et al. (2001) measured an extent 11.6 × 3.3 arcmin^2 at a major axis position angle of 45°. Thus, we derive a similar major-axis extent as Ott et al. (2001) but a slightly larger minor axis extent.

The continuum emission associated with the optical disc of the galaxy is shown in Fig. 13. The continuum is very extended and follows the optical disc of the galaxy, though its radial extent is much less than that of the optical disc. It is characterized by a bright central core with a peak flux density of 3.74 Jy beam^{-1}. In addition, there is a moderately bright, localized continuum emission along the major axis of the galaxy. Finally, a small extension of weak emission (which looks like an asymmetric double horned profile) is seen on the South-East side of the galaxy. Symmetric to that (with respect to the major axis), there seems to be a (finger-like) extension, although it is very weak. These may be signatures of outflows caused by star formation activity. We show a plot of the central continuum emission in Fig. 13. Our observation does not resolve the very compact nuclear core of NGC 4945. Ott et al. (2001) found a source size of 7.6 × 3.4 arcsec^2. However, to get the central flux distribution at our resolution, we show a plot of the flux density as a function of position along a slice taken at a major axis position angle of 45° in Fig. 13. The profile has a bright narrow core and faint broad wings. We fit a double Gaussian function to the profile and derived a dispersion of σ = 15.4 arcsec. As shown in Fig. 13, most of the emission in the core is contained within a diameter of twice this value, about 31 arcsec (1 kpc at 6.7 Mpc).

To calculate the total continuum flux, first, we blank all continuum emission not associated with the galaxy using the MIRIAD task IMMASK. After that, we sum all the remaining non-blanked pixels and convert the unit from Jy beam^{-1} to Jy. We derive a total flux density of 6.2 Jy, of which 90 per cent resides within a radius of 332 arcsec (10.8 kpc). Thus, we recover ∼ 26 per cent more flux than Ott et al. (2001). A plot of the continuum map at the highest resolution (7.2 × 6.3 arcsec^2) is shown in the Appendix.

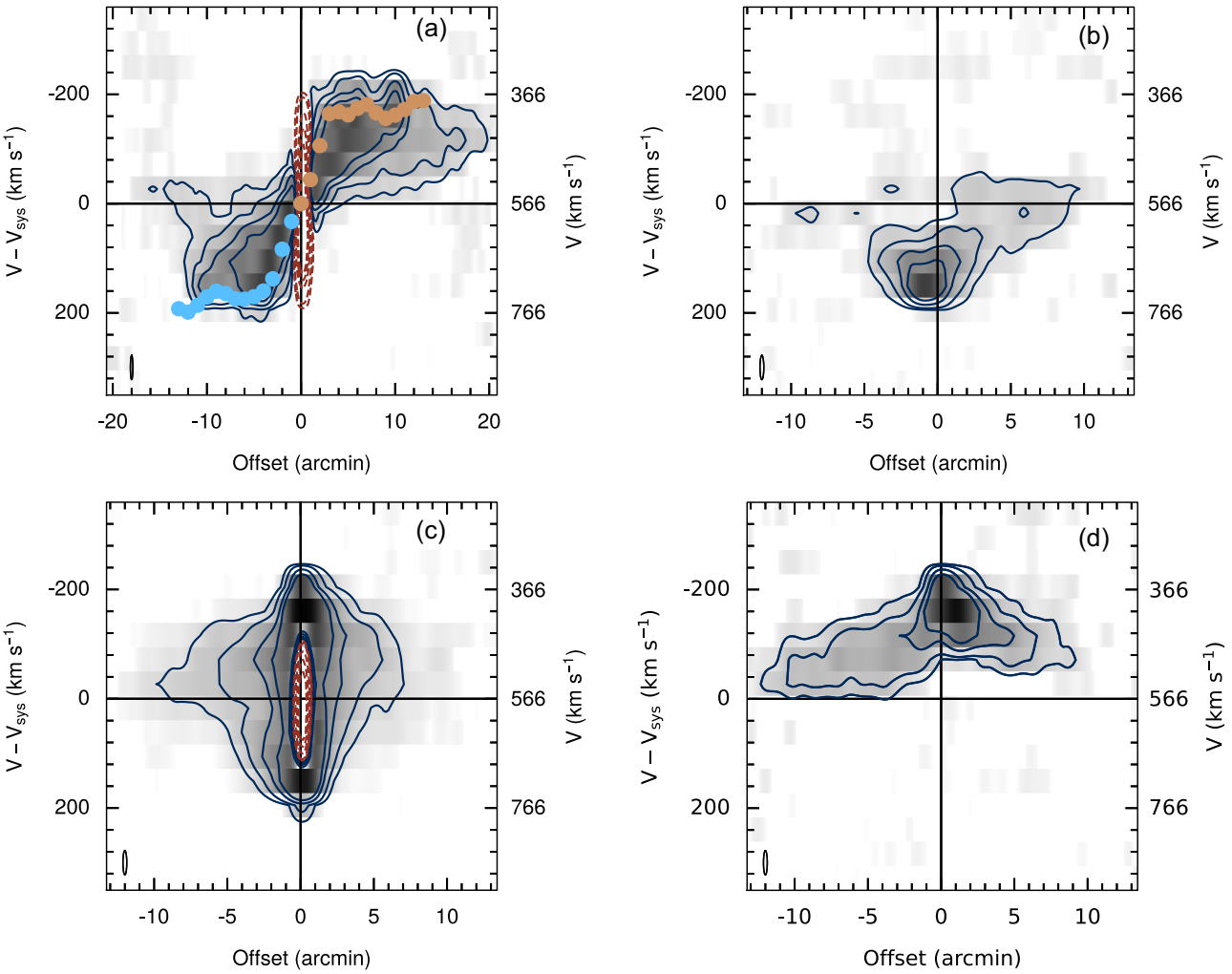

Figure 10. MeerKAT H I position–velocity diagrams of NGC 4945 taken along slices A, B, C, and D as shown in Fig. 8. Blue solid contours: H I emission; the contour levels are (2.5, 6, 14, 24, 100) × rms, where rms is equal to 0.2 mJy beam^{-1}. The circle symbols at the upper left-hand panel show the TIRIFIC model rotation curve. Red dashed contours: H I absorption; the contour levels are (–14.0, –10.0, –6.0, –2.0, –0.8) mJy beam^{-1}. The elongated ellipses at the lower left-hand corners of the plots show the size of the beam FWHM = 60 arcsec (along the *x*-axis) and the channel spacing (along the *y*-axis).

3.5.2 Star formation

The radio continuum emission at 1.4 GHz can be used to trace recent star formation since it is dominated by synchrotron radiation from supernovae remnants and thermal emission from H II regions (Liu, Gao & Greve 2015). To convert the 21-cm continuum to an SFR, we first convert the continuum flux to luminosity using the following relation from Yun, Reddy & Condon (2001) and Martinsson et al. (2016)

$$\log L_{1.4\mathrm{GHz}}[\mathrm{W\,Hz^{-1}}] = 20.08 + 2\log D[\mathrm{Mpc}] + \log S_{1.4\mathrm{GHz}}[\mathrm{Jy}], \quad (4)$$

where D is the distance in Mpc, $L_{1.4\mathrm{GHz}}$ is the radio continuum luminosity in W Hz^{-1}, and $S_{1.4\,\mathrm{GHz}}$ is the total flux density in Jy. We derive $L_{1.4\mathrm{GHz}} = 3.3 \times 10^{22}$ WHz^{-1}. The radio continuum luminosity is known to correlate with far-infrared (FIR) luminosity, indicating a strong correlation between star formation and cosmic ray production (Yun et al. 2001 and references therein). Yun et al. (2001) analysed the FIR-radio continuum luminosity of 1809 IRAS 2 Jy sample galaxies taken from the 1.2 Jy IRAS Redshift Survey catalogue (Strauss et al. 1992), and found the following best-fitting correlation

$$\log L_{1.4\mathrm{GHz}} = (0.99 \pm 0.01)\log(L_{60\,\mu\mathrm{m}}/\mathrm{L}_\odot) + (12.07 \pm 0.08). \quad (5)$$

NGC 4945 has a nuclear FIR luminosity of $4 \times 10^{10}\,\mathrm{L}_\odot$. Using the above correlation, this corresponds to a 1.4-GHz luminosity of $L_{1.4\mathrm{GHz}} = 3.7 \times 10^{22}$ [W Hz^{-1}], which agrees with our observed value of $L_{1.4\,\mathrm{GHz}} = 3.3 \times 10^{22}$ [W Hz^{-1}]. We convert $L_{1.4\,\mathrm{GHz}}$ to SFR using the radio flux calibration of Bell (2003; see also Liu et al. 2015) given by

$$\mathrm{SFR_{RC}}[\mathrm{M_\odot yr^{-1}}] = \begin{cases} 5.52 \times 10^{-22} L_{1.4\mathrm{GHz}} & \text{if } L_{1.4\mathrm{GHz}} > L_C \\ \dfrac{5.52 \times 10^{-22}}{0.1 + 0.9(L/L_C)^{0.3}} L_{1.4\mathrm{GHz}} & \text{if } L_{1.4\mathrm{GHz}} \leq L_C, \end{cases} \quad (6)$$

where $\mathrm{SFR_{RC}}$ is the radio continuum SFR in $\mathrm{M_\odot yr^{-1}}$, and $L_C = 6.4 \times 10^{21}$ W Hz^{-1} is the luminosity of a $\sim L*$ galaxy. Since $L_{1.4\,\mathrm{GHz}} \leq 10^{23}$ for NGC 4945, the bulk of its radio continuum luminosity is expected to come from star formation rather than dominated by radio AGN (Yun et al. 2001). We derive a star formation rate of $\mathrm{SFR_{RC}} = 18.4\,\mathrm{M_\odot\,yr^{-1}}$, 75 per cent of which comes from the core having a diameter of 1 kpc (defined previously as the area containing most of the bright continuum emission). This value is on the low-end of the range observed in starburst galaxies (10–100 $\mathrm{M_\odot}$).

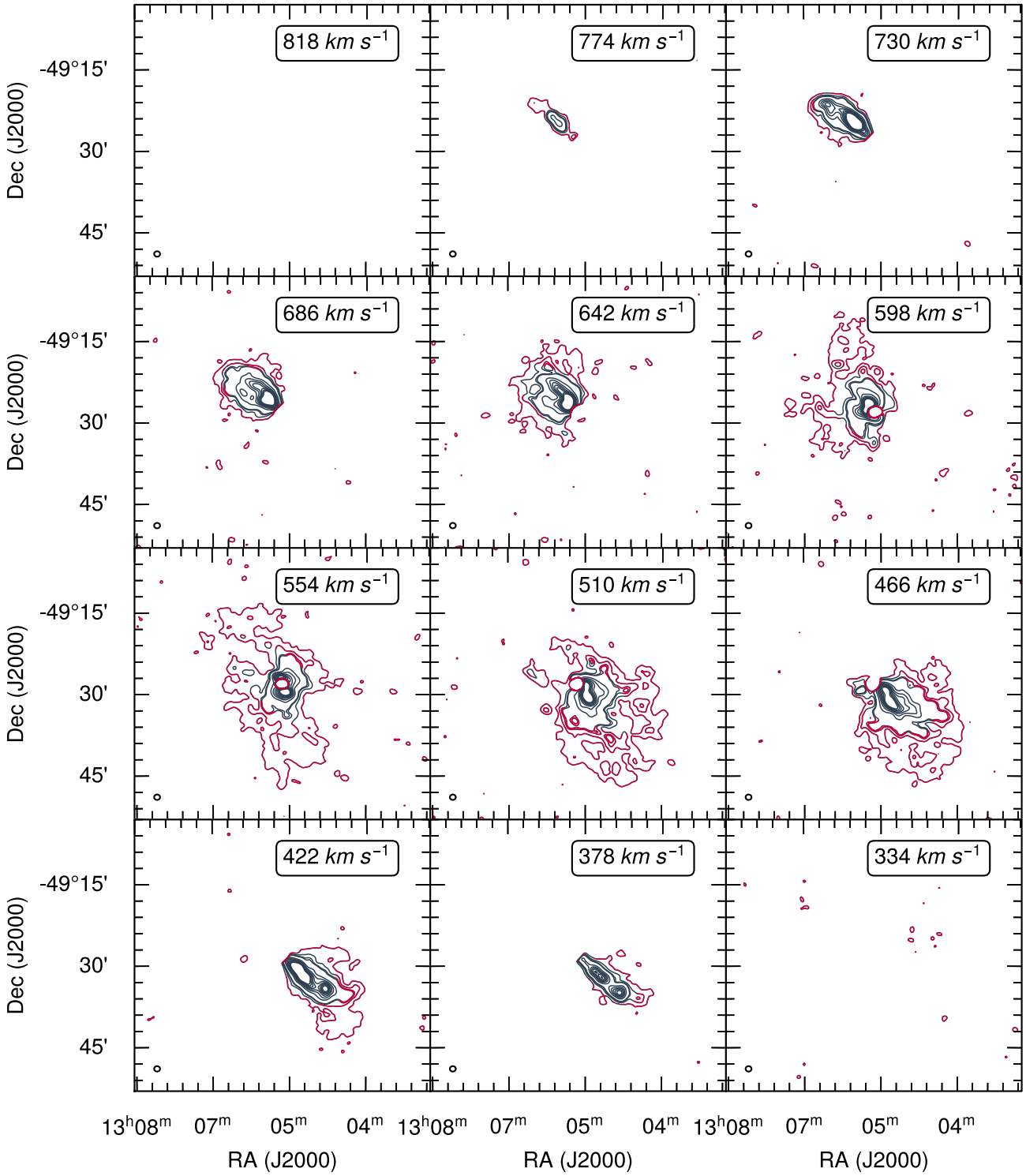

Figure 11. MeerKAT H I channel maps of the nearby starburst galaxy NGC 4945 showing the location of the anomalous gas (red contours) and the gas in the main disc of the galaxy (blue contours). The contour levels range from 3 × rms to 20 × rms in step of 7 × rms and 20 × rms to 400 × rms in step of 20 × rms, where rms is 0.20 mJy beam^{-1}. The black circles shown at the bottom left-hand corner of each panel show the beam (FWHM = 60 arcsec).

4 DISCUSSION

This observation has changed our view of NGC 4945. We have found halo gas around almost the whole disc of the galaxies, not captured by previous H I observations. For future high-spectral resolution observations of this galaxy, it would be possible to do the interactive profile fitting techniques done by Lucero et al. (2015) to separate the anomalous components in the galaxy and study the kinematics of the halo gas in detail. In this study, we have used the kinematic model of the galaxy to isolate the anomalous gas. Halo gas is found in virtually all sides of NGC 4945, with more H I located in the lower left-hand quadrant of the galaxy. Halo gas with asymmetric distribution has previously been found for NGC 253. While Boomsma et al. (2005)

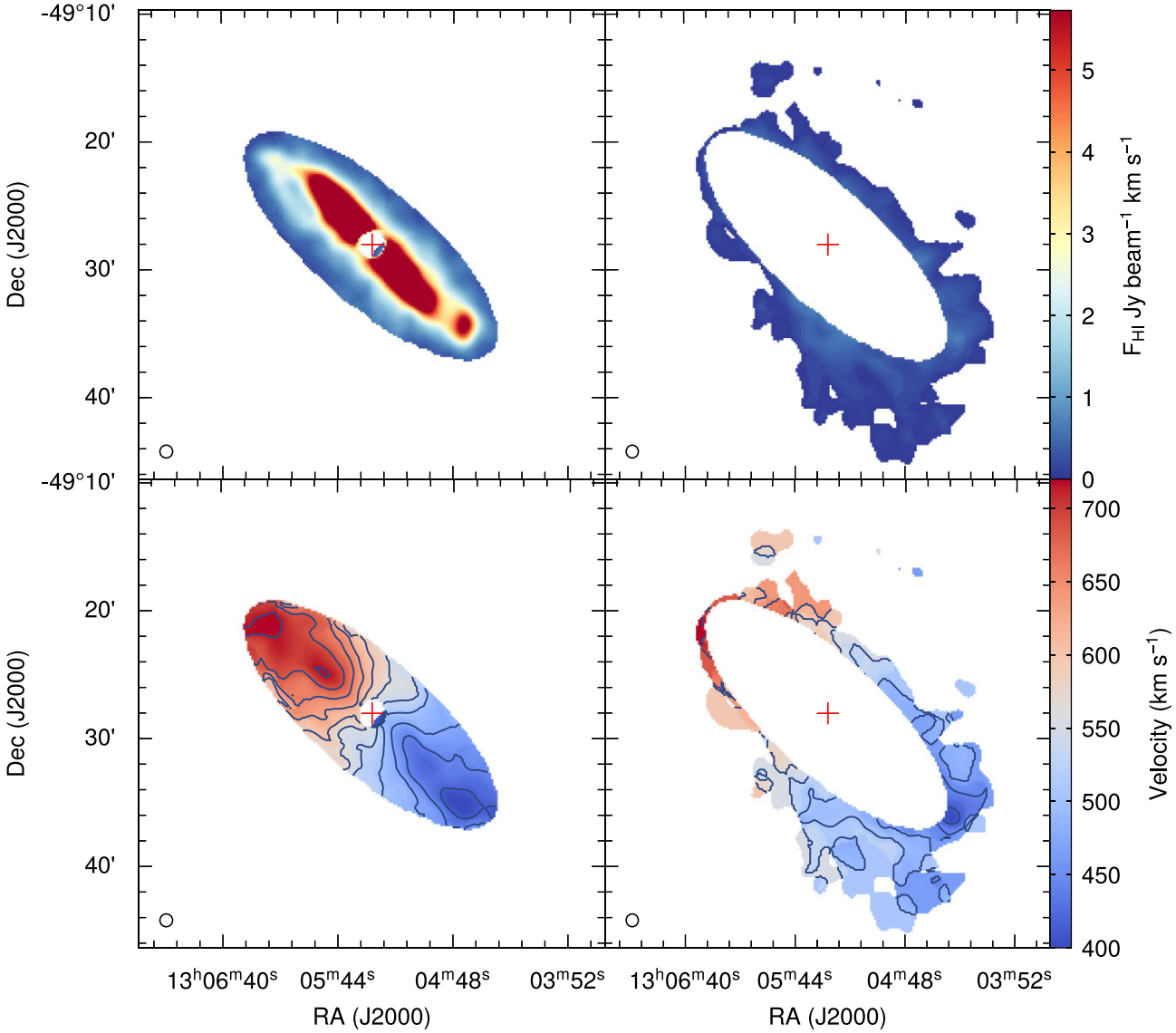

Figure 12. Top left-hand panel: Moment-0 map of the main disc of NGC 4945. Top right-hand panel: Moment-0 map of the anomalous gas in NGC 4945. Bottom left-hand panel: velocity field (Moment-1) of the main disc of NGC 4945. Bottom right-hand panel: velocity field of the anomalous gas in NGC 4945. The contour levels are 385 to 745 km s^{-1} in step of 30 km s^{-1}. The red crosses show the kinematic centre derived from TIRIFIC. The circles at the bottom left-hand corner of each plot show the beam (FWHM = 60 arcsec).

reported that the extra-planar gas in NGC 253 is only found in one side of the galaxy, the more sensitive map by Lucero et al. (2015) showed that the halo gas is also found in the southern part of the galaxy. The distribution is still clearly asymmetric, with the northern side having more anomalous H I than the south side. For the starburst galaxy NGC 253, it was shown that the gas in the halo of NGC 253 has similar kinematics to the gas in the disc but is trailing by 10–20 km s^{-1} (Lucero et al. 2015). Future high-resolution studies of NGC 4945 can confirm if this is also the case for NGC 4945.

Many scenarios are proposed in the literature regarding the origin of gas in the halo of galaxies. These include the interaction of galaxies with a nearby companion or the environment, pristine gas from the cosmic web accreted on to the galaxies, gas being blown out of the disc into the halo by expanding superbubbles created by supernovae and stellar winds (Fraternali & Binney 2006; Sánchez Almeida et al. 2014; Marasco et al. 2019). NGC 4945 belongs to the Centaurus A group, and thus interaction with the intra-group medium may have played a role in forming its halo gas. The likelihood of the halo gas being from the cosmic web is low given the column density level at which we are detecting it. Accretion from the cosmic web is expected to happen at a lower column density level than we are probing. Thus, although we were unable to model the kinematics of the halo gas and compare to simulations, at least part of the halo gas we see here is likely due to outflows driven by the central starburst of the galaxy as seen in NGC 1808 and NGC 253 (Koribalski et al. 1993; Lucero et al. 2015).

The rotation curve of NGC 4945 resembles the overall spiral galaxy populations, most of which are characterized by a steep solid-body inner rotation curve and then flattens out to the outermost observed radius. There are exceptional cases where rotation curves are declining, such as that of NGC 253 (Hlavacek-Larrondo et al. 2011; Lucero et al. 2015), see also the cases for 22 nearby spiral galaxies compiled from the literature by Zobnina & Zasov (2020). We did not find a clear signature of a declining rotation curve for

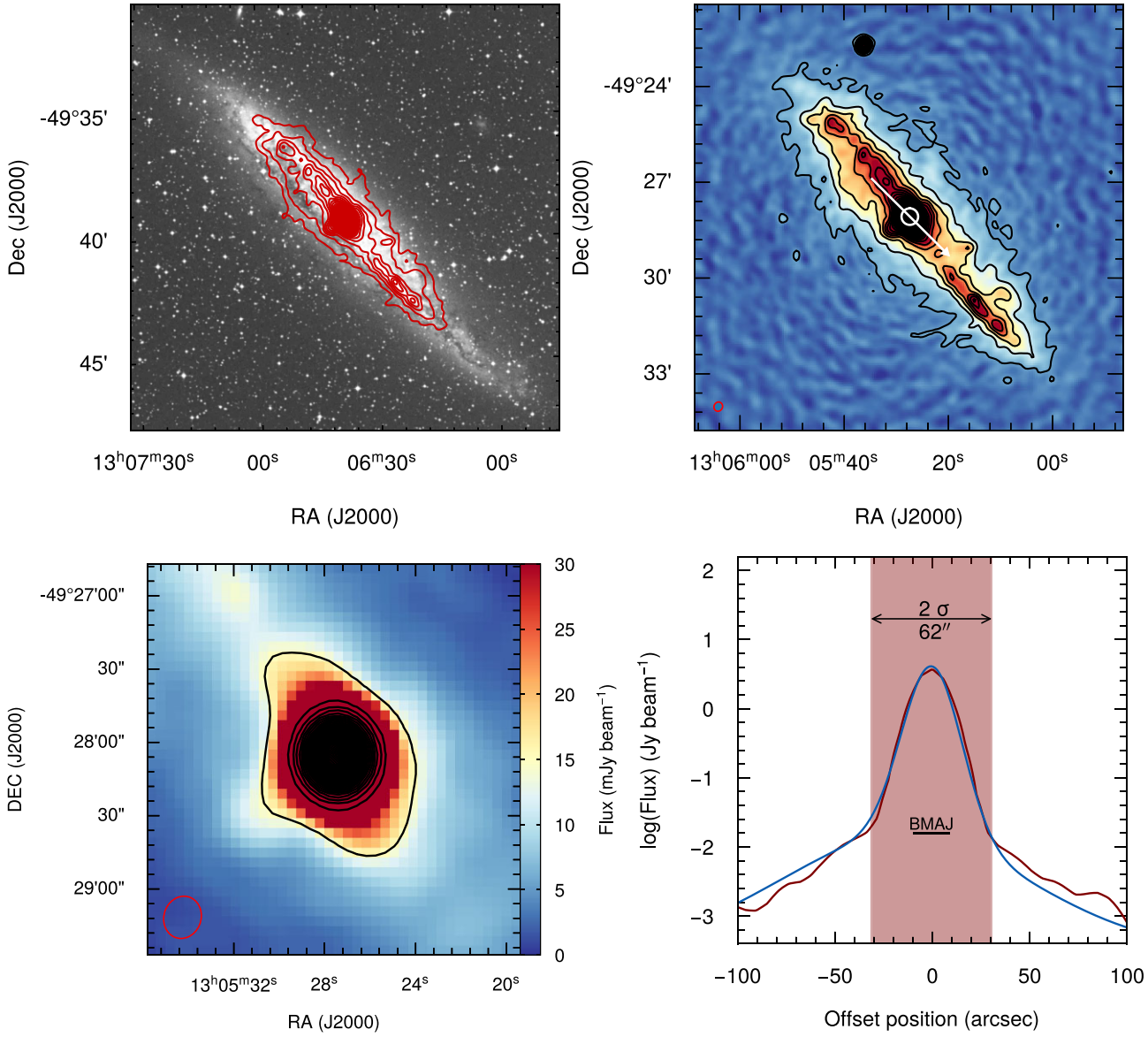

Figure 13. Top left-hand panel: MeerKAT radio continuum contour map of NGC 4945 (red contours) overlaid on to a DSS2 *B*-band optical image (grayscale). The contour levels are 0.00011 to 3.8 Jy beam^{-1} in step of 0.002 Jy beam^{-1}. Top right-hand panel: continuum map of NGC 4945; the contour levels are 0.00011 to 3.8 Jy beam^{-1} in step of 0.002 Jy beam^{-1}. The red ellipse at the bottom left-hand panel corner shows the beam (FWHM=17.6 arcsec). The white arrow, taken at a position angle of 45°, shows the slice from which the profile at the bottom left-hand of the figure was taken. The white circle shows the diameter of the core measured by fitting the profile at the bottom left of the figure with a Gaussian function. The diameter of the core is 31 arcsec. Bottom left-hand panel: the central region of the continuum emission in NGC 4945. The contour levels go from 0.015 to 3.72 Jy beam^{-1} in step of 0.1 mJy beam^{-1}. The red ellipse at the bottom left-hand corner shows the beam (FWHM = 17.6 arcsec). Bottom right-hand panel: flux density as a function of position along the slice shown as the white arrow at the top right-hand panel of the figure, plotted in log-scale to highlight the two discs components. The blue line shows a double Gaussian fit to the profile. The shaded area shows a 2σ width, where σ is the dispersion of the (fitted Gaussian) core component. The value of σ represents the diameter of the core of the disc shown by the white circle at the top right-hand panel of the figure. BMAJ represents the major axis of the beam.

NGC 4945. As explained in Zobnina & Zasov (2020), cares need to be taken when interpreting a declining rotation curve since it does not necessarily indicate the edge of the dark matter halo.

We have fit the receding and the approaching sides of the galaxy separately to derive the rotation curve of NGC 4945. We have found that both sides have an outer warp. The warp on the receding side is more clearly visible in the models and the observed velocity field. The intensity distribution in the receding side appears to be suppressed since it extends just as much as the optical disc. This type of halo asymmetry has been found for NGC 253 (Boomsma et al. 2005). They suggested that such a lack of H I might be caused by ionization resulting from the galaxy's starburst activity. For this to occur, though, the outer layer of the gas needs to be warped, which is the case for NGC 4945. Tidal interactions and ram pressure stripping are among the mechanisms that can cause H I deficiency. Perhaps the warp in the receding side is related to this H I suppression. However, it is worth noting that H I deficient galaxies are not necessarily warped. The origin of a warp is still a subject of intense investigation in the literature (Sánchez-Salcedo 2006; Poggio et al. 2020). Re-observation of this galaxy at higher velocity resolution will enable

us to do proper modelling of the kinematics of the halo gas and investigate its possible origin based on existing models.

5 SUMMARY

We have presented MeerKAT H I maps of the starburst galaxy NGC 4945, revealing for the first time the presence of faint H I emission in its outskirts. The halo gas accounts for about 6.8 per cent of the galaxy's total mass. This is thanks to the sensitivity of MeerKAT, enabling us to go down to a 3σ column density level of 5×10^{18} cm^{-2}. Despite being a starburst galaxy and the improved sensitivity, the amount of the halo gas in NGC 4945 is within the range found for normal star-forming galaxies. This could indicate that there might be gas expelled from the galaxy into the intergalactic medium due to a starburst-driven superwind (Heckman et al. 2000; Strickland & Stevens 2000). In addition, the halo gas does not seem to follow the kinematics of the disc (such as the trailing gas in NGC 891 or NGC 253), this could be another indication that there might be gas escaping the galaxy. After isolating the area of genuine emission, we derived a total H I flux density of 509 Jy km s^{-1}, which is about 20 per cent higher than the flux density derived by Koribalski et al. (2018) using ATCA mosaic imaging. We have modelled the H I emission through 3D tilted-ring modelling techniques using the TIRIFIC and FAT software (Józsa 2007; Kamphuis et al. 2015). The halo gas does not follow the regular kinematics of the main disc of the galaxy, and our attempt to fit it with TIRIFIC failed. Therefore, we have only made the kinematic modelling of the main disc of the galaxy. The modelling indicates the presence of a warp on the approaching and the receding sides of the galaxy. We derive a flat rotation curve with $v_{\rm flat} = 176$ km s^{-1} for the approaching side and $v_{\rm flat} = 188$ km s^{-1} for the receding side, in agreement with Kamphuis et al. (2015). Due to our coarse velocity resolution, only areas of bright H I emission were modelled here. Strong H I absorption seen throughout the entire velocity range seen in H I emission, is present towards the nuclear region of NGC 4945. The absorption lines appear to be broad and asymmetric, indicating the presence of a fast rotating ring and outflowing gas from the nuclei. The existence of a fast rotating ring is further supported by the clear rotation pattern in the absorption velocity field of NGC 4945. This fast rotation can be caused by the interaction of the surrounding neutral gas with the AGN at the centre of NGC 4945. A similar case has been found for NG 1808 by Koribalski et al. (1993). We have also presented a map of the radio continuum emission, most of which is associated with the bright optical disc of NGC 4945. The continuum emission is very extended and characterized by a bright central core with a diameter of about 0.6 kpc. The continuum flux suggests that NGC 4945 is forming stars at a global rate of 18.4 M$_\odot$ yr^{-1}, 75 per cent of which resides within a core radius of 1 kpc.

ACKNOWLEDGEMENTS

We would like to thank the anonymous referee for a careful reading of the manuscript and very useful comments, which greatly improved the presentation of the paper.

RI acknowledges financial support from grant RTI2018-096228-B-C31 (MCIU/AEI/FEDER,UE) and from the State Agency for Research of the Spanish Ministry of Science, Innovation and Universities through the 'Center of Excellence Severo Ochoa' awarded to the Instituto de Astrofísica de Andalucía (SEV-2017-0709), from the grant IAA4SKA (Ref. R18-RT-3082) from the Economic Transformation, Industry, Knowledge and Universities Council of the Regional Government of Andalusia and the European Regional Development Fund from the European Union.

The MeerKAT telescope is operated by the South African Radio Astronomy Observatory, which is a facility of the National Research Foundation, an agency of the Department of Science and Innovation.

This work is based upon research supported by the South African Research Chairs Initiative of the Department of Science and Technology and National Research Foundation.

The financial assistance of the South African Radio Astronomy Observatory (SARAO) towards this research is hereby acknowledged (www.sarao.ac.za).

At Ruhr University Bochum, this research is supported by BMBF Verbundforschung grant 05A20PC4 and by DFG Sonderforschungsbereich SFB1491.

This project has received funding from the European Research Council (ERC) under the European Union's Horizon 2020 research and innovation programme grant agreement no. 882793, project name MeerGas.

This project has received funding from the European Research Council (ERC) under the European Union's Horizon 2020 research and innovation programme (grant agreement no. 679627; project name FORNAX).

DATA AVAILABILITY

The data from this study are available upon request to the corresponding author, Roger Ianjamasimanana.

REFERENCES

Baan W. A., 1985, Nature, 315, 26
Bell E. F., 2003, ApJ, 586, 794
Bergman P., Aalto S., Black J. H., Rydbeck G., 1992, A&A, 265, 403
Boissier S., Prantzos N., Boselli A., Gavazzi G., 2003, MNRAS, 346, 1215
Boomsma R., Oosterloo T. A., Fraternali F., van der Hulst J. M., Sancisi R., 2005, A&A, 431, 65
Coziol R., 1996, A&A, 309, 345
Cunningham M. R., Whiteoak J. B., 2005, MNRAS, 364, 37
Curran S. J., Johansson L. E. B., Bergman P., Heikkilä A., Aalto S., 2001, A&A, 367, 457
Dahlem M., Golla G., Whiteoak J. B., Wielebinski R., Huettemeister S., Henkel C., 1993, A&A, 270, 29
de Blok W. J. G. et al., 2018, ApJ, 865, 26
de Blok W. J. G. et al., 2020, A&A, 643, A147
de Vaucouleurs G., 1964, ApJ, 139, 899
de Vaucouleurs G., de Vaucouleurs A., Corwin Herold G. J., Buta R. J., Paturel G., Fouque P., 1991, Third Reference Catalogue of Bright Galaxies, Vol.82. Springer, New York, NY, p. 621
Done C., Madejski G. M., Smith D. A., 1996, ApJ, 463, L63
Elmouttie M., Haynes R. F., Jones K. L., Ehle M., Beck R., Harnett J. I., Wielebinski R., 1997, MNRAS, 284, 830
Emig K. L. et al., 2020, ApJ, 903, 50
Field G. B., 1959, ApJ, 129, 536
Fraternali F., Binney J. J., 2006, MNRAS, 366, 449
Fraternali F., Oosterloo T., Sancisi R., van Moorsel G., 2001, ApJ, 562, L47
Freyer T., Hensler G., Yorke H. W., 2003, ApJ, 594, 888
Gentile G. et al., 2013, A&A, 554, A125
Geréb K., Maccagni F. M., Morganti R., Oosterloo T. A., 2015, A&A, 575, A44
Hagiwara Y., Horiuchi S., Doi A., Miyoshi M., Edwards P. G., 2016, ApJ, 827, 69
Heald G. et al., 2011, A&A, 526, A118
Heckman T. M., 2003, Rev. Mex. Astron. Astrofis., 17, 47
Heckman T. M., Lehnert M. D., Strickland D. K., Armus L., 2000, ApJS, 129, 493

Henkel C., Whiteoak J. B., Mauersberger R., 1994, A&A, 284, 17
Henkel C. et al., 2018, A&A, 615, A155
Hitschfeld M. et al., 2008, A&A, 479, 75
Hlavacek-Larrondo J., Carignan C., Daigle O., de Denus-Baillargeon M. M., Marcelin M., Epinat B., Hernandez O., 2011, MNRAS, 411, 71
Humphreys E. M. L., Vlemmings W. H. T., Impellizzeri C. M. V., Galametz M., Olberg M., Conway J. E., Belitsky V., De Breuck C., 2016, A&A, 592, L13
Ianjamasimanana R. et al., 2020, MNRAS, 497, 4795
Irwin J. A. et al., 2011, MNRAS, 410, 1423
Irwin J. et al., 2012, AJ, 144, 44
Ishizuki S., Kawabe R., Ishiguro M., Okumura S. K., Morita K.-I., 1990, Nature, 344, 224
Józsa G. I. G., 2007, A&A, 468, 903
Józsa G. I. G. et al., 2020, Astrophysics Source Code Library, record ascl: 2006.014
Józsa G. I. G. et al., 2021, MNRAS, 501, 2704
Kamphuis P., Józsa G. I. G., Oh S. H., Spekkens K., Urbancic N., Serra P., Koribalski B. S., Dettmar R. J., 2015, MNRAS, 452, 3139
Kanekar N., Braun R., Roy N., 2011, ApJ, 737, L33
Karachentsev I. D. et al., 2007, AJ, 133, 504
Kenyon J. S., Smirnov O. M., Grobler T. L., Perkins S. J., 2018, MNRAS, 478, 2399
Koornneef J., 1993, ApJ, 403, 581
Koribalski B., 1996, in Skillman E. D., ed., ASP Conf. Ser. Vol. 106, The Minnesota Lectures on Extragalactic Neutral Hydrogen. Astron. Soc. Pac., San Francisco, p. 238
Koribalski B., Dickey J. M., Mebold U., 1993, ApJ, 402, L41
Koribalski B. S. et al., 2004, AJ, 128, 16
Koribalski B. S. et al., 2018, MNRAS, 478, 1611
Leroy A. K., Walter F., Brinks E., Bigiel F., de Blok W. J. G., Madore B., Thornley M. D., 2008, AJ, 136, 2782
Liu L., Gao Y., Greve T. R., 2015, ApJ, 805, 31
Lucero D. M., Carignan C., Elson E. C., Randriamampand ry T. H., Jarrett T. H., Oosterloo T. A., Heald G. H., 2015, MNRAS, 450, 3935
McMullin J. P., Waters B., Schiebel D., Young W., Golap K., 2007, in Shaw R. A., Hill F., Bell D. J., eds, ASP Conf. Ser. Vol. 376, Astronomical Data Analysis Software and Systems XVI. Astron. Soc. Pac., San Francisco, p. 127
Marasco A. et al., 2019, A&A, 631, A50
Martini P., Leroy A. K., Mangum J. G., Bolatto A., Keating K. M., Sandstrom K., Walter F., 2018, ApJ, 856, 61
Martinsson T. P. K., Verheijen M. A. W., Bershady M. A., Westfall K. B., Andersen D. R., Swaters R. A., 2016, A&A, 585, A99
Mayya Y. D., Bressan A., Carrasco L., Hernand ez-Martinez L., 2006, ApJ, 649, 172
Mould J., Sakai S., 2008, ApJ, 686, L75
Noordam J. E., Smirnov O. M., 2010, A&A, 524, A61
Offringa A. R., 2012, PhD thesis, Univ. Groningen
Offringa A. R. et al., 2014, MNRAS, 444, 606
Oosterloo T., Fraternali F., Sancisi R., 2007, Astron. J., 134, 1019
Ott M., Whiteoak J. B., Henkel C., Wielebinski R., 2001, A&A, 372, 463
Poggio E., Drimmel R., Andrae R., Bailer-Jones C. A. L., Fouesneau M., Lattanzi M. G., Smart R. L., Spagna A., 2020, Nature Astron., 4, 590
Roy A. L., Oosterloo T., Goss W. M., Anantharamaiah K. R., 2010, A&A, 517, A82
Ryder S. D., Buta R. J., Toledo H., Shukla H., Staveley-Smith L., Walsh W., 1996, ApJ, 460, 665
Sánchez Almeida J., Elmegreen B. G., Muñoz-Tuñón C., Elmegreen D. M., 2014, A&A Rev., 22, 71
Sánchez-Salcedo F. J., 2006, MNRAS, 365, 555
Sault R. J., Teuben P. J., Wright M. C. H., 1995, in Shaw R. A., Payne H. E., Hayes J. J. E., eds, ASP Conf. Ser. Vol. 77, Astronomical Data Analysis Software and Systems IV. Astron. Soc. Pac., San Francisco, p. 433
Serra P. et al., 2015, MNRAS, 448, 1922
Shapiro P. R., Field G. B., 1976, ApJ, 205, 762
Sorgho A., Foster T., Carignan C., Chemin L., 2019, MNRAS, 486, 504
Strauss M. A., Huchra J. P., Davis M., Yahil A., Fisher K. B., Tonry J., 1992, ApJS, 83, 29
Strickland D. K., Stevens I. R., 2000, MNRAS, 314, 511
Swaters R. A., Sancisi R., van der Hulst J. M., 1997, ApJ, 491, 140
Temple R. F., Raychaudhury S., Stevens I. R., 2005, MNRAS, 362, 581
Vargas C. J. et al., 2017, ApJ, 839, 118
Venturi G. et al., 2018, AGN13: Beauty and the Beast. agn_13, 50
Westmeier T., Jurek R., Obreschkow D., Koribalski B. S., Staveley-Smith L., 2014, MNRAS, 438, 1176
Whiteoak J. B., Bunton J. D., 1985, Proc. Astron. Soc. Australia, 6, 171
Yun M. S., Ho P. T. P., Lo K. Y., 1994, Nature, 372, 530
Yun M. S., Reddy N. A., Condon J. J., 2001, ApJ, 554, 803
Zhang Z.-Y., Romano D., Ivison R. J., Papadopoulos P. P., Matteucci F., 2018, Nature, 558, 260
Zobnina D. I., Zasov A. V., 2020, Astron. Rep., 64, 295

APPENDIX A: ADDITIONAL FIGURES

In this Appendix, we show additional figures that complement the main section of the paper. The channel maps of NGC 4945 from the high-resolution data cube (7.5×6.4 arcsec^2) is shown in Fig. A1. As mentioned previously, even at this resolution, the fluffy faint H I emission is already visible. The top left-hand panel of Fig. A2, illustrates how we determine the extent of the H I disc as explained in Section 3.2 of the paper. Similarly, the top right-hand panel of Fig. A2 shows an illustration of the estimation of the extent of the continuum map as mentioned in Section 3.5. To show the size of the continuum map relative to the size of the H I disc of NGC 4945, we overlay the continuum map on top of its H I surface density map. Finally, a high resolution version of the continuum map, i.e. at a resolution of 7.3×6.2 arcsec^2 is shown at the bottom right-hand of Fig. A2.

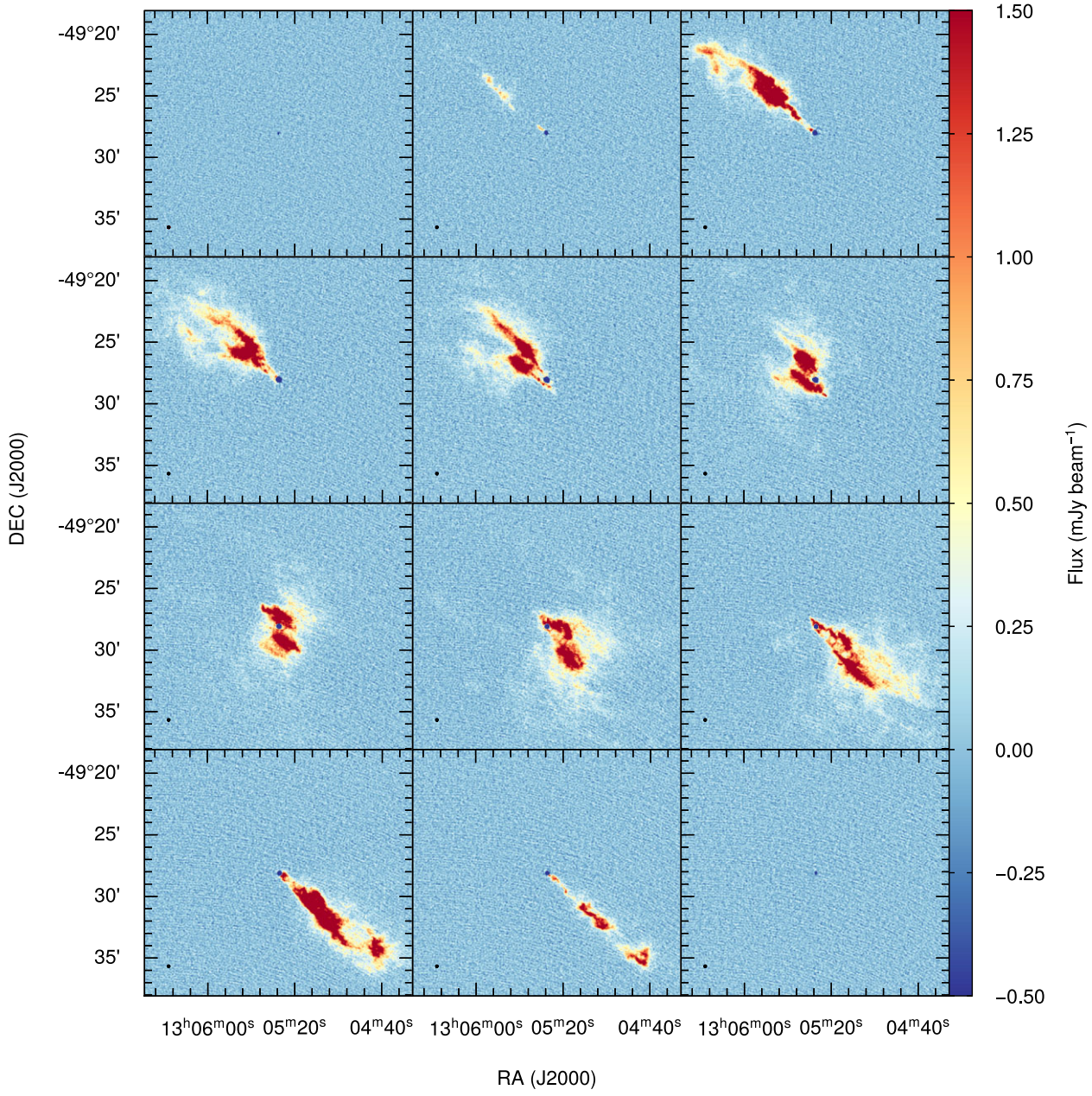

Figure A1. MeerKAT H I channel maps of NGC 4945 at a resolution of 7.5 × 6.4 arcsec^2. The size of the beam is represented by the small dots at the bottom left-hand corner of each panel.

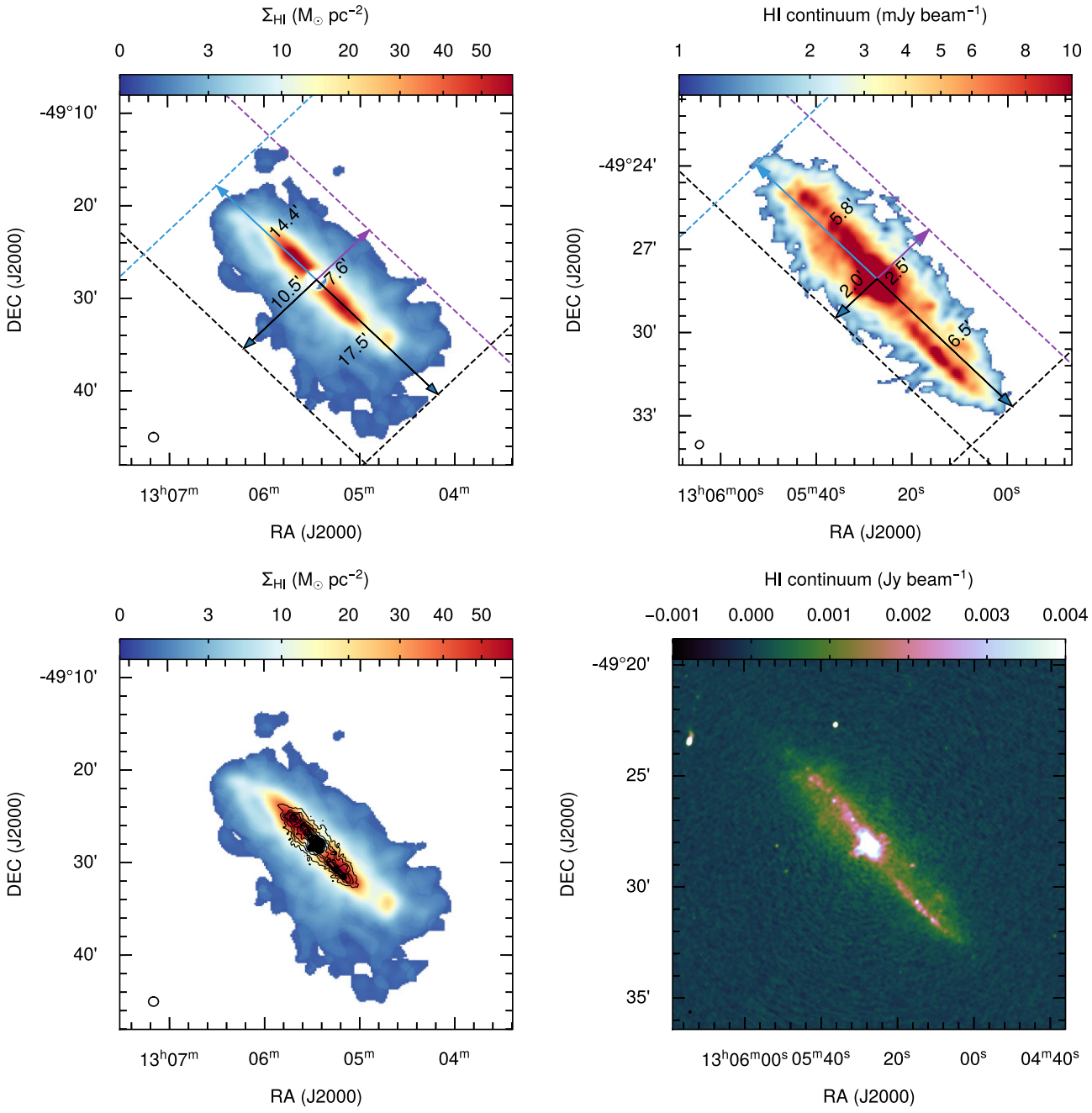

Figure A2. Top left-hand panel: H I surface density map of NGC 4945, arrows and dashed lines indicate the extent of the H I disc. The beam is shown by the black circle at the bottom left-hand corner of the plot (FWHM = 60 arcsec). Top right-hand panel: continuum map of NGC 4945, arrows and dashed lines indicate the extent of the continuum emission. The beam is shown by the black ellipse at the bottom left-hand corner of the plot ($FWHM_{BMAJ} \times FWHM_{BMIN}$ = 17.6 × 15.8 arcsec^2). Bottom left-hand panel: H I surface density map (coloured image) and the continuum map of NGC 4945 (black contours). The contour levels range from 0.0001 to 3 Jy beam^{-1} in step of 0.0015 Jy beam^{-1}. The black circle at the bottom left-hand corner of the plot shows the beam (FWHM = 60 arcsec). Bottom right-hand panel: the radio continuum map of the galaxy at a resolution of 7.3 × 6.2 arcsec^2. The beam is shown at the bottom left-hand corner of the plot but is very small so it is not visible.

This paper has been typeset from a TEX/LATEX file prepared by the author.